

# Geometric Modeling of Hippocampal Tau Deposition: A Surface-Based Framework for Covariate Analysis and Off-Target Contamination Detection

Liangkang Wang<sup>1</sup>, Akhil Ambekar<sup>1</sup>, Ani Eloyan<sup>1\*</sup>,<sup>\*\*</sup>

<sup>1</sup>Department of Biostatistics, Brown University

\*Correspondence: [ani\\_eloyan@brown.edu](mailto:ani_eloyan@brown.edu)

\*\* Data used in preparation of this article were obtained from the Alzheimer's Disease Neuroimaging Initiative (ADNI) database ([adni.loni.usc.edu](http://adni.loni.usc.edu)). As such, the investigators within the ADNI contributed to the design and implementation of ADNI and/or provided data but did not participate in analysis or writing of this report.

A complete listing of ADNI investigators can be found at:

[http://adni.loni.usc.edu/wpcontent/uploads/how\\_to\\_apply/ADNI\\_Acknowledgement\\_List.pdf](http://adni.loni.usc.edu/wpcontent/uploads/how_to_apply/ADNI_Acknowledgement_List.pdf)

December 3, 2025

**Abstract:** We introduce a novel framework combining geometric modeling with disease progression analysis to investigate tau deposition in Alzheimer's disease (AD) using positron emission tomography (PET) data. We focus on the hippocampus—a region of the brain affected early in AD—and construct a principal surface such that the projection of voxels onto this surface captures the spatial distribution and morphological changes of tau pathology. We use bidirectional projection distances and interpolated standardized uptake value ratio (SUVR) values to map tau PET data onto this surface, enabling quantification of coverage, intensity, and thickness. The projection provides a low-dimensional embedding space, reducing potential issues related to multiple comparisons while preserving spatial specificity. To analyze covariate effects, we apply a two-stage regression model with inverse probability weighting to adjust for signal sparsity and selection bias. Using the SuStain model, we

identify subtypes and stages of AD and investigate tau dynamics related to AD subtypes. We find that the limbic-predominant subtype exhibits age-associated, nonlinear accumulation patterns in coverage and thickness, while the posterior subtype shows more uniform SUVR increases across progression. Model-based predictions further reveal that tau deposition within the hippocampus follows a structured spatial trajectory, originating centrally and expanding bidirectionally with increasing thickness in one subtype, while our second identified subtype exhibits earlier tau involvement in the posterior hippocampus—consistent with their respective whole-brain subtype definitions. Finally, we demonstrate that directional signal patterns on the principal surface can be used to detect potential contamination from the adjacent choroid plexus, highlighting the broader applicability of our framework. We validate the proposed framework, by running the analysis for amyloid PET modeling, thus showing its applicability in another modality.

**Keywords:** Imaging statistics, Manifold Learning, Medial Skeleton, Alzheimer’s Disease, tau PET

## 1 Introduction

Alzheimer’s disease (AD) is a progressive neurodegenerative disorder and the leading cause of dementia worldwide, accounting for approximately 60–80% of all cases (Better, 2023). AD is characterized by the accumulation of tau protein and beta-amyloid plaques in the brain (La Joie et al., 2020). Tau protein deposition plays a critical role in neuronal damage and disease progression. Current methods quantify tau deposition using standardized uptake value ratio (SUVR) from positron emission tomography (PET) scans (Joseph, 2004; Pemberton et al., 2022), but primarily focus on regional or global SUVR comparisons (Theriault et al., 2022; Vogel et al., 2021). However, these approaches often overlook the spatial distribution and morphological variations of tau protein deposition, limiting their ability to characterize disease progression comprehensively. Prior studies have also highlighted variability in tau biomarker levels across different populations, raising concerns about the applicability of global SUVR thresholds (Lah et al., 2024). These findings underscore the need for a more localized and structurally informed quantification approach for fine-grained tau analysis.

Voxel-wise analysis of tau PET data has been widely adopted to map spatial patterns of pathology (Ossenkoppele et al., 2020; Waragai et al., 2009). While such methods offer fine-grained resolution, they face key limitations: multiple comparisons burden, spatial noise, and lack of anatomical interpretability. In particular, voxel-wise approaches often ignore the intrinsic geometry of curved brain structures, such as

the hippocampus, making it difficult to capture smooth and consistent patterns of tau deposition. From a biological perspective, tau accumulation is unlikely to increase linearly with disease progression; rather, pathological effects are believed to emerge only once local SUVR exceeds a critical threshold (Chen, Lu, et al., 2021). Yet, most voxel- and region-based analyses assume a linear relationship between SUVR and disease severity, overlooking this threshold-driven transition. How spatially localized tau accumulation emerges and expands along disease progression therefore remains poorly understood, motivating our geometry-aware analysis of its spatial distribution and morphological trajectory.

In this study, we propose a manifold representation (m-rep) framework (see **Section 2.2** for methodological details) to quantify the spatial distribution and morphological changes in tau deposition. Specifically, we represent each subject's tau PET signal on an anatomically aligned principal surface using features that encode suprathreshold coverage, signal intensity, and local geometry. To enable biologically meaningful and geometrically consistent surface construction, we employ a two-step approach: extracting a medial skeleton using the outward flux method, followed by principal surface fitting. Covariate effects on the derived spatial features are subsequently assessed using two-stage regression with inverse probability weighting (Hernan, 2024), though these biomarkers can be used in other settings depending on the specific analysis objectives.

AD is known to exhibit substantial clinical and pathological heterogeneity, particularly in how tau deposition patterns evolve across individuals. Emerging evidence suggests that AD comprises multiple subtypes that are characterized by different spatial trajectories of tau spread (Vogel et al., 2021). Traditional approaches, such as group-level averaging or voxel-wise analysis, primarily compare tau accumulation across broad diagnostic categories (e.g., cognitively normal, mild cognitive impairment (MCI), AD) and implicitly assume a single, homogeneous disease trajectory. Such methods fail to capture subtype-specific differences in both the spatial distribution and progression dynamics of tau pathology. To explicitly account for this population-level heterogeneity, we applied the Subtype and Stage Inference (SuStIn) algorithm (Young et al., 2018) to estimate each participant's disease subtype and stage based on regional SUVR profiles. Incorporating these latent variables enables our geometric framework to distinguish subtype-specific spatial patterns and to relate morphological trajectories to disease progression.

Our surface representation and spatial feature extraction approach enables spatially localized modeling of hippocampal tau pathology. Stage and subtype covariates derived using SuStIn are incorporated in subsequent analyses. Our primary objective in this study is to characterize subtype-specific tau deposition patterns and their progression dynamics, shedding light on the heterogeneity of AD. To this end, our analyses focus on modeling spatial deposition patterns—specifically, signal intensity and surface morphology—and their relationships with disease stage and subtype. While developed in the context of

hippocampal tau pathology, the approach is readily extendable to other imaging applications.

In addition to capturing biologically meaningful patterns of tau deposition, the proposed framework also enables the identification of off-target contamination from the choroid plexus (CP)—a well-known confound in hippocampal tau PET imaging (Pawlik et al., 2020; Wolters et al., 2020). The CP is a highly vascularized structure adjacent to the hippocampus that exhibits strong nonspecific tracer binding, particularly for ligands such as  $^{18}\text{F}$ -AV-1451. Because of its high signal intensity and close anatomical proximity, CP activity can leak into the hippocampal region during image preprocessing and registration, leading to apparent tau elevation or suppression unrelated to true pathology. Such misregistration effects are exacerbated in the elderly and populations with neurodegenerative disease, where ventricular enlargement increases spatial variability of the CP (Eisma et al., 2024). By analyzing directional signal asymmetries and spatial gradients on the hippocampal principal surface, our framework localizes CP spill-in effects and quantifies their dependence on disease diagnosis, illustrating its broader utility for artifact detection and quality assessment in PET imaging.

## 2 Materials and Methods

In this section, we describe the data source, the overall workflow of our proposed approach, and the methodological framework for surface representation and feature extraction, followed by the derivation of disease subgroup and stage using SuStAln and statistical analyses used in downstream modeling. For the analysis described in this manuscript, we used data from the Alzheimer’s Disease Neuroimaging Initiative (ADNI), which is a landmark study launched in 2003 with the goal of collecting and sharing data to have the means of developing biomarkers for disease progression evaluation, characterization of AD, and treatment development. The study data collection protocols, documentation, and data dictionaries are available at [adni.loni.usc.edu](http://adni.loni.usc.edu). We briefly describe our selection of variables and imaging used in this paper, further details can be found in ADNI data dictionaries.

### 2.1 Data Source and Preprocessing

**Sample characteristics** In the analysis, we included PET-MRI pairs from 628 participants from the ADNI study (Petersen et al., 2010; Weber et al., 2021), each with T1-weighted MRI acquired within two years of the corresponding tau PET scan. Of these, 150 were cognitively normal (CN), 272 had MCI, and 206 were diagnosed with AD. The sample included 292 males and 336 females, with a mean age of 75.1 years (SD = 7.6, range = 55.2–94.4 years). Table 1 describes the general demographic characteristics

by study group for the participants included in the final sample.

Table 1: Baseline characteristics by diagnosis

	<b>CN (N=304)</b>	<b>MCI (N=218)</b>	<b>AD (N=106)</b>	<b>Total (N=628)</b>
<b>Age (years)</b>				
Mean (SD)	74.6 (7.20)	74.9 (7.68)	76.7 (8.16)	75.1 (7.56)
Median [Min, Max]	74.3 [55.2, 94.4]	74.8 [55.5, 93.2]	76.6 [55.7, 92.0]	75.2 [55.2, 94.4]
<b>Sex</b>				
Female	158 (52.0%)	77 (35.3%)	53 (50.0%)	288 (45.9%)
Male	146 (48.0%)	141 (64.7%)	53 (50.0%)	340 (54.1%)
<b>APOE <math>\epsilon</math>4 Carrier</b>				
Non-carrier	182 (59.9%)	95 (43.6%)	26 (24.5%)	303 (48.2%)
Carrier	92 (30.3%)	62 (28.4%)	41 (38.7%)	195 (31.1%)
Missing	30 (9.9%)	61 (28.0%)	39 (36.8%)	130 (20.7%)

**Image acquisition and preprocessing** All scans were pre-processed following the standard ADNI pipeline. Acquisition protocols for MRI and PET, as well as details on pre-processing procedures are described in detail at <https://adni.loni.usc.edu/>. Briefly, tau PET images were first co-registered to the corresponding native-space T1-weighted MRI, and then non-linearly warped to the MNI152 template space to ensure consistent anatomical alignment across subjects. SUVR images were computed using the cerebellar gray matter as the reference region, and partial volume correction was applied to reduce spill-over effects. A random subset of images from each scanner model was visually inspected to verify registration quality and confirm the absence of major motion artifacts. To account for potential site-related variability, we applied the neuroCombat algorithm (Fortin, 2024) to correct for scanner- and protocol-induced batch effects. Scans were grouped by scanner model, with rare models (fewer than five scans) merged by manufacturer. Age, sex, and diagnosis were included as biological covariates in the harmonization model to preserve meaningful variance while removing non-biological noise.

**Hippocampal Structure and Tau Signal Definition** For spatial localization, hippocampal geometry was defined using the MNI152-space T1-weighted MRI automated anatomical labeling (AAL) atlas (Rolls et al., 2015). The hippocampal region defined in this atlas was used to construct a medial surface representation, which served as a shared spatial surface for projecting tau PET signals. Since all PET images were non-linearly registered to the MNI152 template, this surface-based framework enabled consistent, anatomically grounded comparison of tau deposition patterns across study participants. To identify regions with significant tau deposition, we applied a fixed thresholding procedure to each participant’s PET

SUVR image. Voxels with SUVR values exceeding 2.0—approximately two standard deviations above the mean regional SUVR—were considered positive for tau signal. This subject-specific binary mask was then projected onto the medial hippocampal surface for downstream shape-based analysis. This threshold was adopted from the SuStaln model (see Section 2.5) and provided a biologically meaningful cutoff for downstream analysis.

## 2.2 Workflow Overview

In this study, we present a novel workflow for analyzing subject-specific tau deposition patterns and structural features in both the left and right hippocampus. The workflow presented in Figure 1 integrates data pre-processing, geometric modeling and feature extraction, and statistical analysis. We process individual PET scans to extract tau signal distributions projected onto a shared medial surface, enabling consistent per-subject shape characterization. By anchoring the analysis in this anatomically consistent coordinate system, we are able to aggregate subject-level representations and conduct group-wise comparisons. This design supports biologically interpretable feature extraction, which serves as the basis for downstream regression modeling. The modules and steps of the workflow are illustrated in Figure 1.

**Module A: Geometric Surface Modeling and Feature Extraction:** The core methodological framework consists of geometric surface modeling and spatial feature extraction. We transform the 3D voxel-wise tau PET signal within the hippocampus into a structured 2D representation on a medial principal surface. Surface construction involves two steps: (1) extracting a medial skeleton using a flux-based thinning algorithm applied to the atlas-defined hippocampal structure, and (2) fitting a smooth principal surface via thin-plate spline (TPS) regularization. Directly applying principal surface fitting to the complex hippocampal geometry often produced convoluted, self-folding surfaces; thus, our two-step approach ensured biologically meaningful and geometrically consistent surface modeling. After aligning subject-level tau PET data to the MNI152 space, suprathreshold tau signals are projected and interpolated onto this shared surface, enabling consistent per-subject shape characterization and group-wise comparisons. This transformation reduces data dimensionality, while preserving the anatomically grounded spatial organization of tau signals. From the projected data, we derive standardized spatial features including suprathreshold coverage, SUVR intensity, and projection-based thickness.

**Module B: Subtype and Stage Classification with SuStaln:** To stratify heterogeneity in tau progression, we applied the Subtype and Stage Inference (SuStaln) algorithm to derive disease subtype and stage for each participant. SuStaln, a widely adopted method in AD research, uses z-score thresholds and

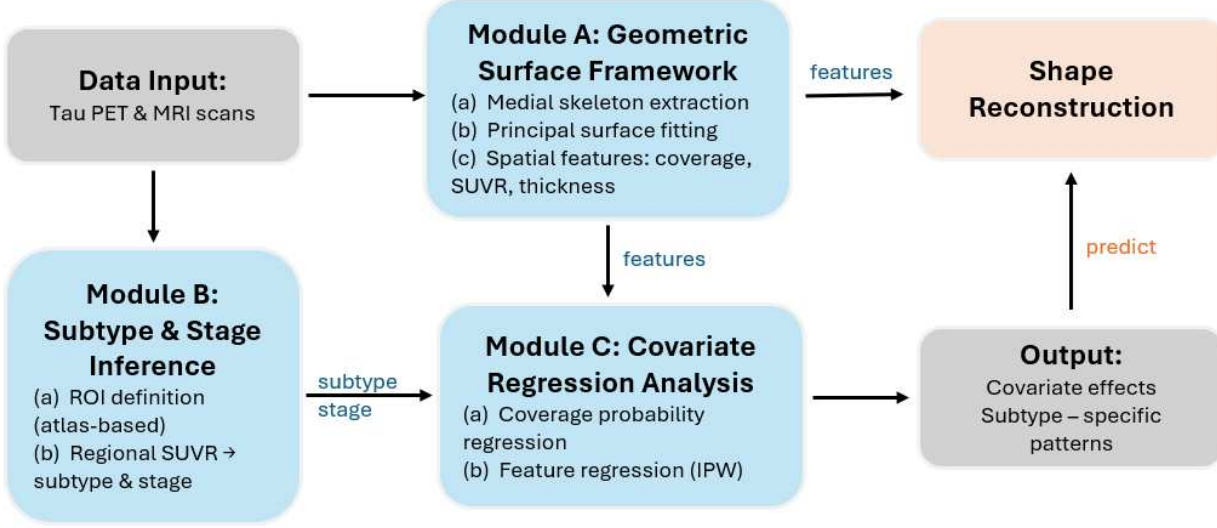


Figure 1: Workflow for spatial tau feature extraction, subtype modeling, and regression analysis. The proposed framework consists of a fixed Geometric Surface Framework (Module A: Geometric Surface Modeling) and two downstream analysis modules (Module B and Module C). Module B: Subtype & Stage Inference applies SuStaln to atlas-defined regional SUVR values to derive disease subtype and stage labels. Module C: Regression Analysis evaluates the effects of demographic and clinical variables on spatial tau features via (a) coverage probability modeling and (b) inverse probability weighted (IPW) regression. This workflow supports both shape reconstruction from geometric features and subtype-specific covariate effect analysis, enabling detailed investigation of heterogeneous spatial tau deposition patterns.

regional severity scores to model disease progression trajectories and has been instrumental in identifying biologically meaningful AD subtypes. Although not part of the core geometric framework, we compared our estimated tau deposition patterns between the SuStaln subtypes and stages.

**Module C: Modeling of Spatial Tau Deposition:** Following feature extraction, we performed a two-stage regression analysis to examine differences of tau deposition between AD subtypes and stages on tau deposition patterns. Covariate-by-subtype interaction terms were included to enable formal comparison of subtype-specific effects. In the first stage, we estimated the probability of suprathreshold signal coverage at each uniformly sampled location on the principal surface, while in the second stage we modeled the effects of demographic and disease-related covariates—including age, sex, diagnosis, and SuStaln-derived stage—on SUVR intensity and projection-based thickness. To mitigate selection bias from conditioning on signal presence, inverse probability weighting (IPW) was applied. This approach allows for robust estimation of both signal intensity and morphological variation, accounting for spatial sparsity and subtype-specific heterogeneity across spatially consistent surface points.

This workflow was applied to both left and right hippocampi as a case study, demonstrating its utility in quantifying and comparing tau pathology across subtypes and stages. While developed for hippocampal tau analysis, the workflow is generalizable and can be extended to other brain regions or disease types, providing a robust approach for analyzing structural and pathological heterogeneity.

## 2.3 Notation and Definitions

To ensure consistency throughout this paper, we adopt the following notations, with descriptive definitions to clarify their roles in the study:

- $R_0 \subset \mathbb{R}^3$  denotes the fixed 3D “template region” of interest, e.g. the hippocampal volume defined by the AAL atlas used in this paper. Its boundary surface  $S_0$  serves as the domain for constructing a medial representation and projecting PET signal.
- $R \subset \mathbb{R}^3$  is a subject-specific shape derived from thresholded tau PET signal. Its boundary  $S$  may be refined or degenerate to a point, and is used for computing coverage, thickness, or spatial distribution differences relative to  $S_0$ .
- $\mathbf{q}_i = (x_i, y_i, z_i) \in R$  denotes the coordinates of a discrete voxel within the tau-positive region  $R$ , where  $i = 1, \dots, V$ , and  $V$  is the total number of sampled points. Each point is associated with a standardized uptake value ratio (SUVR), representing tau signal intensity. The matrix  $\mathbf{q} = \{\mathbf{q}_1, \dots, \mathbf{q}_V\}$  is the full set of voxel coordinates used for surface projection and geometric processing.
- $D(\mathbf{q}_i)$  is the Euclidean distance from voxel  $\mathbf{q}_i$  to the reference surface  $S_0$ , defined as  $D(\mathbf{q}_i) = \|\mathbf{q}_i - \pi(\mathbf{q}_i)\|_2$ , where  $\pi(\mathbf{q}_i)$  is the orthogonal projection of  $\mathbf{q}_i$  onto  $S_0$ .
- $\dot{\mathbf{q}} = \nabla D(\mathbf{q}) = (\partial_x D, \partial_y D, \partial_z D)$  denotes the gradient vector field of the distance function, indicating the local direction of maximal increase of distance, which in this context points inward from the boundary toward the interior. The vector field is normalized such that  $\|\dot{\mathbf{q}}_i\| = 1$ .
- $\Phi(\mathbf{q}_i)$  is the average outward flux of the gradient vector field  $\dot{\mathbf{q}}$  at location  $\mathbf{q}_i$ . It is defined in the continuous setting as the limit of the average directional projection over a vanishing spherical neighborhood as follows.

$$\Phi(\mathbf{q}) = \lim_{\varepsilon \rightarrow 0} \frac{1}{|\partial B_\varepsilon(\mathbf{q})|} \int_{\mathbf{p} \in \partial B_\varepsilon(\mathbf{q})} \langle \dot{\mathbf{q}}(\mathbf{p}), \mathbf{n}_\mathbf{p} \rangle \, dS(\mathbf{p}), \quad (1)$$

where  $B_\varepsilon(\mathbf{q})$  denotes a closed ball of radius  $\varepsilon$  centered at  $\mathbf{q}$ ,  $\partial B_\varepsilon(\mathbf{q})$  is its boundary surface,  $\mathbf{n}_p$  is the unit outward normal vector at  $\mathbf{p} \in \partial B_\varepsilon(\mathbf{q})$ , orthogonal to the local tangent plane of the spherical surface, and  $dS$  is the surface area element. The flux quantifies the local directional consistency of  $\mathbf{q}$ . Values of  $\Phi(\mathbf{q})$  near zero correspond to homogeneous regions, while strictly negative values are indicative of medial skeleton points—locations equidistant from multiple boundary regions where the vector field is highly divergent.

- In this study, we distinguish between two types of unit normal vectors.  $\mathcal{N}_{MS}$  represents the normal vector associated with the medial skeleton, defined as the vector from the center of the maximal inscribed sphere to its tangent point on the boundary surface  $S_0$ .  $\mathcal{N}_{PS}$  is the normal vector of the principal surface, defined as the unit vector orthogonal to the local tangent plane at a point on the surface. Although  $\mathcal{N}_{MS}$  and  $\mathcal{N}_{PS}$  originate from distinct geometric definitions, they are closely aligned in practice, because the principal surface is constructed as a smooth approximation along the medial skeleton. Accordingly, we treat them as directionally equivalent and use  $\mathcal{N}$  to denote either (see Section 2.4.3) unless otherwise specified.
- $\mathbf{t}_i = (t_{i1}, t_{i2}) \in [0, 1] \times [0, 1]$  is used as 2D parameterization coordinates for the principal surface, which map each point on the principal surface to its corresponding position in a normalized 2D space.
- $f : \mathbb{R}^2 \rightarrow \mathbb{R}^3$  represents a smooth mapping function representing the principal surface in 3D space. It maps 2D parameterization coordinate  $\mathbf{t}_i$  to its corresponding point  $\mathbf{q}_i$  on the principal surface.
- $\lambda_f : \mathbb{R}^3 \rightarrow \mathbb{R}^2$  is a projection function that maps a 3D point  $\mathbf{q}_i$  onto the parameterization space  $\mathbf{t}_i$ , identifying the closest corresponding point on the principal surface.

## 2.4 Geometric Surface Modeling and Feature Extraction

We developed a geometric surface modeling framework to represent subject-specific tau deposition within the hippocampus. This approach—corresponding to Module A of our overall workflow shown in Figure 1, in which we integrate medial skeleton extraction and principal surface (PS) fitting to create an anatomically aligned, low-dimensional representation. The resulting medial representation (m-rep) enables standardized spatial feature extraction across individuals, including suprathreshold coverage, SUVR intensity, and projection-based thickness, forming the basis for subsequent analyses.

### 2.4.1 Medial Skeleton Extraction via Outward Flux

Accurately capturing the intrinsic geometry of the hippocampus is essential for modeling spatial patterns of tau deposition. As the first component of our geometric modeling framework (Module A-a in Figure 1), we construct a medial skeleton to provide a compact, anatomically meaningful representation of hippocampal shape. The medial skeleton is identified using an average outward flux criterion, guided by the classical grassfire flow model (Blum, 1967). This model conceptualizes the inward propagation of a shape’s boundary at constant speed along the inward normal vector, with the medial skeleton emerging where inward-propagating fronts meet. While the grassfire flow has traditionally been formulated using Hamilton-Jacobi equations (Bouix et al., 2005; Siddiqi et al., 2002), we implement a direct, flux-based approach better suited for discrete imaging data (Bouix et al., 2003). Specifically, we compute the average outward flux  $\Phi(\mathbf{q}_i)$  at each voxel  $\mathbf{q}_i$  within tau-positive regions by evaluating the average directional relationship between the local distance gradient field  $\dot{\mathbf{q}}(\mathbf{p})$  and the outward normal vector  $\mathbf{n}_p$  over a small spherical neighborhood using equation (1). In regions where the gradient directions are locally consistent (e.g., homogeneous interior areas), flux values approach zero. In contrast, at medial skeleton locations where inward gradients from opposing boundaries diverge, the flux becomes strictly negative, indicating high local symmetry and local divergence (Bouix et al., 2003). This criterion is particularly robust for complex topological shapes such as PET-derived tau deposition.

**Discrete Implementation** Following this criterion, we now describe the discrete implementation used to approximate flux values within the tau-positive region. Specifically, we estimate flux over a discrete spherical shell of radius  $\varepsilon$  centered at  $\mathbf{q}_i$ , using  $K$  uniformly sampled surface points  $\{\mathbf{p}_k\}_{k=1}^K$ . Each direction  $\mathbf{p}_k$  contributes a directional projection of the local gradient field onto the corresponding outward normal vector:

$$\Phi(\mathbf{q}_i) \approx \frac{1}{K} \sum_{k=1}^K \left\langle \dot{\mathbf{q}}(\mathbf{p}_k), \frac{\mathbf{p}_k - \mathbf{q}_i}{\|\mathbf{p}_k - \mathbf{q}_i\|} \right\rangle.$$

We classify  $\mathbf{q}_i$  as a medial point if  $\Phi(\mathbf{q}_i) < \tau_{\text{flux}}$ , with a default threshold of  $\tau_{\text{flux}} = -0.2$  selected based on empirical separation between medial and background regions (Siddiqi et al., 2002).

**Point-wise Resolution Enhancement** To support robust flux computation in sparse PET-derived masks, we increase point sampling density using point-wise interpolation. Since flux estimation relies on evaluating local neighborhoods around each voxel, the native PET resolution often leads to sparse coverage, which can reduce numerical stability and spatial continuity. To address this, we insert two evenly spaced points between each pair of adjacent voxels in 3D space, effectively tripling the resolution.

This empirical strategy—corresponding to a 1/3 interval ratio—was found to preserve the structural integrity of the medial skeleton and support smoother downstream principal surface fitting.

### 2.4.2 Principal Surface Fitting

To smooth the discrete and irregular medial skeleton derived from flux computation, we applied a principal surface fitting method proposed by Yue et al., 2016. This step (Module A-b in Figure 1) regularizes the geometry and establishes a continuous two-dimensional parameterization of the hippocampal structure. The resulting parameter space facilitates spatial alignment, dimensionality reduction, and consistent representation of tau deposition patterns across individuals. We first centered and projected the medial skeleton points in  $\mathbb{R}^3$  onto their first two principal components using principal component analysis (PCA). The resulting coordinates captured the dominant geometric variation and were standardized to the domain  $[0, 1] \times [0, 1]$ , providing an initial two-dimensional parameterization consistent with downstream interpolation and analysis. We then applied a bivariate thin-plate spline (TPS) to fit a smooth principal surface, minimizing penalized least-squares error to achieve geometric regularization (Wood et al., 2016). The TPS produced a smooth mapping  $f: \mathbb{R}^2 \rightarrow \mathbb{R}^3$  from 2D parameter space to the 3D surface points:

$$\mathbf{q}_i = f(\mathbf{t}_i) = \begin{bmatrix} \hat{f}_{11}(t_{i1}) + \hat{f}_{12}(t_{i2}) + \hat{f}_{13}(t_{i1}, t_{i2}) \\ \hat{f}_{21}(t_{i1}) + \hat{f}_{22}(t_{i2}) + \hat{f}_{23}(t_{i1}, t_{i2}) \\ \hat{f}_{31}(t_{i1}) + \hat{f}_{32}(t_{i2}) + \hat{f}_{33}(t_{i1}, t_{i2}) \end{bmatrix},$$

where  $\mathbf{t}_i = (t_{i1}, t_{i2}) \in \mathbb{R}^2$  are the 2D parameter values corresponding to 3D coordinates  $\mathbf{q}_i$  on the principal surface. This parameterization step provides a smooth and consistent mapping from the medial skeleton to the principal surface.

Once the initial surface  $f(\mathbf{t}_i)$  was fitted, each medial skeleton point  $\mathbf{q}_i$  was projected onto the current principal surface using the projection function  $\lambda_f$ , which identified the closest point on the surface

$$\lambda_f(\mathbf{q}_i) = \sup_t \{t : \|\mathbf{q}_i - f(t)\| = \inf_\mu \|\mathbf{q}_i - f(\mu)\|\}.$$

In cases where multiple parameterizations  $t$  yielded identical projection distances, the largest  $t$  value was selected to ensure consistent mapping and to resolve potential non-uniqueness in the projection, following the original implementation by Yue et al., 2016. The parameterization was then iteratively updated until changes across iterations fell below a predefined threshold. This iterative refinement ensured that the final principal surface accurately represented the medial skeleton geometry and provided a stable parameterization for subsequent spatial feature extraction.

### 2.4.3 Projection and Feature Extraction

To ensure standardized feature extraction across participants (Module A-c in Figure 1), we first projected all suprathreshold tau-PET points ( $SUVR > 2.0$ ) onto the shared principal surface. The PS was derived from the atlas-defined hippocampal structure through medial skeleton extraction and principal surface fitting (see Sections 2.4.1 and 2.4.2). Each PET voxel was projected to its nearest point on the PS based on Euclidean distance.

**SUVR Interpolation** To construct reference anchors for surface-based interpolation, we uniformly sampled 235 fixed grid points on the left PS and 262 on the right to ensure coverage on both sides of the principal surface and spatial uniformity. These numbers were specific to fit the hippocampal surface and can be adjusted for other regions depending on their geometry and spatial extent. At each reference location  $\mathbf{t}_0 \in \mathbb{R}^2$ , SUVR values were estimated using LOESS interpolation (Cleveland et al., 1992). We denote by  $s(\mathbf{t})$  the scalar SUVR value associated with the PS location  $f(\mathbf{t}) \in \mathbb{R}^3$ . Thus  $f(\cdot)$  always refers to the three-dimensional coordinate map of the principal surface, while  $s(\cdot)$  denotes the scalar field of SUVR defined on the same parameter domain. The LOESS interpolation is applied to suprathreshold projected points  $\{(\mathbf{t}_i, s(\mathbf{t}_i))\}$ , minimizing  $\hat{s}(\mathbf{t}_0) = \arg \min_{\beta_0, \beta} \sum_{i=1}^N w_i(\mathbf{t}_0) (s(\mathbf{t}_i) - \beta_0 - \beta^\top (\mathbf{t}_i - \mathbf{t}_0))^2$ , where  $w_i(\mathbf{t}_0)$  is a tricube weight decreasing with distance from  $\mathbf{t}_0$ , and the interpolated SUVR at  $\mathbf{t}_0$  is given by  $\hat{s}(\mathbf{t}_0) = \beta_0$ . Interpolation is limited to regions with sufficient local data support (Figure 2b-d). Following SUVR interpolation, boundary points from the tau-PET mask are projected onto the PS to compute geometric projection distances. These distances are interpolated at the same grid points for downstream analysis.

**Projection-Based Shape Representation** The spatial features—including suprathreshold coverage, interpolated SUVR intensity, and bidirectional projection distances—provide a compact yet comprehensive characterization of tau deposition. At each grid point, we denote by  $D(\mathbf{t})$  the signed projection distance from the PS to the hippocampal boundary along the intrinsic normal vector, and negative distance as the distance in the opposite direction. These directional measurements capture local thickness and anisotropy of deposition patterns and are interpolated at the same grid points for downstream shape analysis.

Together, these features support both feature-based statistical modeling and surface-based shape reconstruction. For example, by combining the 2D parameter coordinates  $\mathbf{t}_i$ , their corresponding surface normals, and interpolated projection distances, we can reconstruct the full tau deposition boundary for the right hippocampus (Figure 2g) as  $\hat{\mathbf{q}}_i = f(\mathbf{t}_i) + D(\mathbf{t}_i) \cdot \mathcal{N}_{\mathbf{t}_i}$ . This reconstruction demonstrates that the geometry and thickness of tau accumulation can be faithfully recovered from the principal surface

representation. By integrating projection-based features with the anatomical alignment of the PS, our medial representation (m-rep) preserves sufficient structural detail for both visualization and statistical modeling.

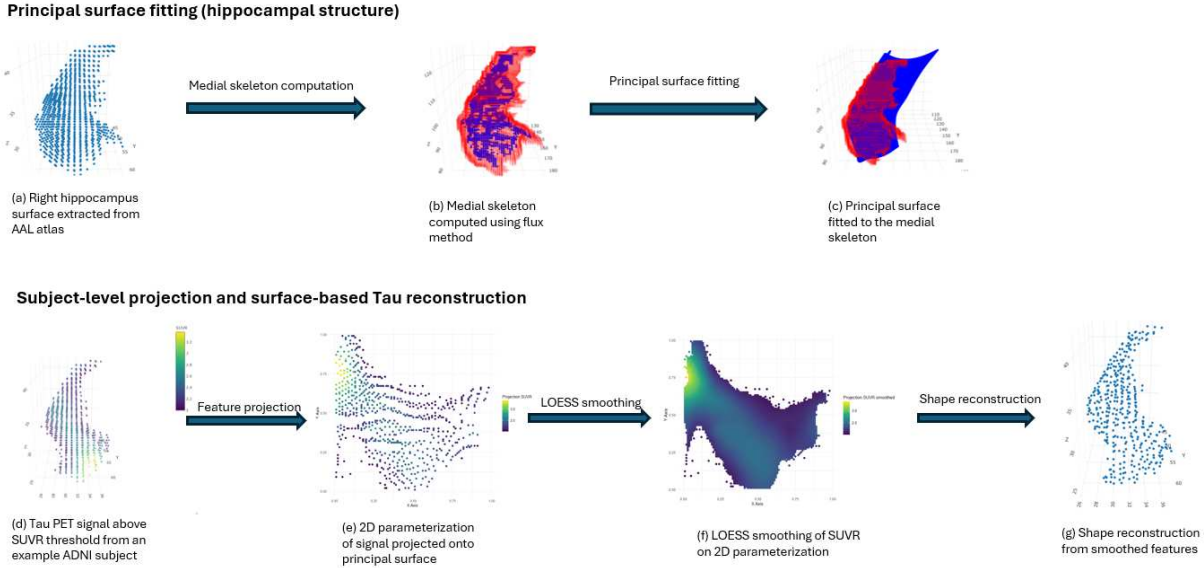


Figure 2: Framework for medial surface-based feature extraction from hippocampal tau PET data. (a) The right hippocampus structure was extracted from an anatomical atlas. (b) A medial skeleton was computed using the outward flux method to capture the intrinsic shape geometry. (c) A principal surface was fitted to the medial skeleton to provide a smooth 2D representation. (d) Tau PET SUVR signals above threshold from an example ADNI participant were identified within the hippocampal structure. (e) These signals were projected onto the principal surface and parameterized in two dimensions. (f) LOESS smoothing was applied to the projected SUVR values to visualize spatial patterns of tau accumulation across the 2D surface. (g) A 3D hippocampal tau surface was reconstructed from the smoothed 2D feature representation, providing subject-level visualization of tau deposition. The arrows indicate the sequential processing steps from anatomical surface extraction to signal projection and interpolation.

## 2.5 Disease Subtype and Stage Modeling with SuStain

To characterize heterogeneous patterns of tau progression, we applied the Subtype and Stage Inference (SuStain) model (Young et al., 2018) to derive subtype and stage classifications. SuStain infers disease subtypes and progression stages by simultaneously clustering and staging subjects based on regional SUVR variation. We implemented the model using its publicly available Python package (Aksman et al., 2021). Following prior studies (Rolls et al., 2015), we constructed a subject-by-feature matrix using mean SUVR values from 10 consolidated regions of interest (ROIs) defined by the AAL atlas. For each ROI, SUVR values were standardized into z-scores across subjects, and two binary indicators ( $z$

$> 2$  and  $z > 5$ ) were computed, resulting in 20 binary features per subject. The optimal number of subtypes ( $k = 4$ ) was selected via ten-fold cross-validation based on the lowest CVIC and out-of-sample likelihood. This solution aligned with previous findings (Vogel et al., 2021), identifying two dominant patterns in the ADNI dataset (Petersen et al., 2010; Weber et al., 2021): a limbic-predominant subtype and an occipitotemporal/posterior variant. Each participant was assigned a most likely subtype and a disease stage (1–20), representing sequential tau accumulation across ROIs. These SuStAln-derived classifications were used in downstream regression analyses, enabling subtype-specific comparisons and stage-based trajectory modeling.

## 2.6 Association between diagnosis and disease stage with tau pathology controlling for demographic covariates

To investigate how demographic and clinical variables influence hippocampal tau pathology, we performed pointwise regression analyses on spatial tau features across the hippocampal surface. Analyses were conducted at 497 uniformly sampled locations on the principal surface (235 left, 262 right), corresponding to the projection grid points defined during surface reconstruction (see Section 2.4.3). Due to spatial sparsity in tau accumulation, not all subjects exhibited suprathreshold signal at every location, requiring a modeling framework that accounts for missing data and selection bias. To evaluate whether covariate effects differed significantly across disease subtypes, we employed a unified regression model incorporating covariate-by-subtype interaction terms. The interaction terms captured differences in effect magnitude between subtype 1 and subtype 2, enabling statistical inference on heterogeneity.

**Stage 1: Logistic Regression for Coverage** For each selected voxel on the shared principal surface, we fit a logistic regression model predicting whether the interpolated SUVR exceeded a z-score threshold of  $z \geq 2$ , consistent with the SuStAln staging criteria (see Section 2.5). The predictors included age (continuous), sex (categorical), clinical diagnosis (ordinal: CN, MCI, AD), and SuStAln disease stage, encoded using a second-order polynomial basis, subtype (categorical), and interaction terms between subtype and each covariate. These models estimate the probability of suprathreshold tau signal, modulated by covariates and their interactions with subtype. The predicted probabilities from this stage were used to compute inverse probability weights for downstream analyses.

**Stage 2: Inverse-Probability-Weighted Linear Regression on Tau Features** Conditional on coverage, we modeled covariate effects on three surface-derived features: (1) positive projection distance

(signal expansion above the surface), (2) negative projection distance (signal expansion below the surface), (3) smoothed SUVR values.

As these features are only defined at suprathreshold locations, directly modeling them without correction may induce selection bias. To address this, we applied inverse probability weighting (IPW) (Hernan, 2024), using weights  $w_i = 1/\hat{p}_i$ , where  $\hat{p}_i$  is the predicted probability of signal presence from Stage 1. Weighted least squares regression was then used to estimate covariate effects on the selected features  $\hat{\beta} = \arg \min_{\beta} \sum_{i=1}^n w_i (Y_i - X_i^\top \beta)^2$ , where  $Y_i$  denotes the tau feature and  $X_i$  includes the same covariates, subtype indicator, and interaction terms.

This regression method enables formal statistical comparison of covariate effects across subtypes while correcting for signal-dependent inclusion. P-values from all models were adjusted using the Benjamini–Hochberg (BH) procedure (Benjamini & Hochberg, 1995) across all surface points and hemispheres.

## 2.7 Detection of Choroid Plexus Contamination

In this subsection, we describe the procedure used to detect off-target signal contamination from the CP within the principal surface (PS) framework. We formally define and quantify the effect of CP contamination on hippocampal tau PET measurements. Specifically, we model how registration inaccuracy and spatial signal mixing can introduce systematic SUVR bias and develop regression-based metrics to localize these effects on the hippocampal surface.

### 2.7.1 Modeling Registration-Induced CP Contamination

To formalize this effect, we modeled registration-induced signal leakage using a two-step transformation process typical in PET–MRI alignment. Let  $x$  denote a voxel coordinate in the original PET space. The corresponding PET signal intensity is  $I_{\text{PET}}^{\text{personal}}(x)$ , and the subject's anatomical MRI intensity is denoted by  $I_{\text{MRI}}^{\text{personal}}(x)$ . The rigid transformation  $T_{\text{PET}}$  maps PET space to subject MRI space, such that  $x' = T_{\text{PET}}(x)$ . Next, a non-rigid deformation field  $u(x')$  maps the MRI space to the template space as  $x'' = x' + u(x')$ , where  $x''$  is the voxel coordinate in template space and  $I_{\text{MRI}}^{\text{template}}(x'')$  is the reference template MRI. The full transformation from PET to template space is thus  $x'' = T_{\text{MRI}}(T_{\text{PET}}(x))$ , and the corresponding PET signal in template space becomes:

$$I_{\text{PET}}^{\text{template}}(x'') = I_{\text{PET}}^{\text{personal}}(T_{\text{PET}}^{-1}(T_{\text{MRI}}^{-1}(x''))).$$

In practice, the estimated deformation  $\hat{u}(x')$  may deviate from the true deformation  $u^*(x')$ , leading to a registration error  $\Delta u(x') = \hat{u}(x') - u^*(x')$ . As a result, the PET signal is assigned to a misregistered location  $x''_{\text{misregistered}} = x' + u^*(x') + \Delta u(x')$ , and the retrieved PET signal becomes  $I_{\text{PET}}^{\text{misregistered}}(x'') = I_{\text{PET}}^{\text{personal}}(T_{\text{PET}}^{-1}(T_{\text{MRI}}^{-1}(x''_{\text{misregistered}})))$ .

We define the contamination error at voxel  $x''$  as

$$\Delta_{\text{contamination}}(x'') = I_{\text{PET}}^{\text{misregistered}}(x'') - I_{\text{PET}}^{\text{template}}(x''),$$

which captures the difference between the ideal PET signal and the one affected by registration inaccuracy. This formulation characterizes how spatial misalignments propagate into the PET signal and introduce systematic contamination—particularly problematic in anatomically constrained and signal-sparse regions such as the hippocampus.

We quantified contamination effects from the CP on hippocampal tau PET signal using a regression-based approach within the PS framework. Each SUVR voxel was projected onto the PS and assigned to its nearest selected PS point, and SUVR values from all projected voxels across individuals were aggregated at each surface location. At each PS point, we fit a linear regression model to characterize the relationship between SUVR and projection distance, a proxy for spatial depth relative to hippocampal surface:

$$\text{SUVR} = \beta_0 + \beta_1 \times \text{Projection Distance} + \epsilon.$$

The slope  $\beta_1$  reflects directional signal bias with respect to the CP-facing surface: positive values ( $\beta_1 > 0$ ) indicate higher SUVR near the surface (positive contamination or spill-in), whereas negative values ( $\beta_1 < 0$ ) indicate lower SUVR near the surface (negative contamination or spill-out). For each point, one-sided hypothesis tests were performed to evaluate the presence of positive ( $\beta_1 > 0$ ) or negative ( $\beta_1 < 0$ ) contamination, and false discovery rate (FDR) was controlled using the Benjamini–Hochberg procedure (Benjamini & Hochberg, 1995). To assess reproducibility across individuals, subject-level  $\beta_1$  estimates were further summarized using group-level one-sample  $t$ -tests within each diagnostic group (CN, MCI, and AD). FDR correction was again applied across surface points separately for each direction. This procedure yielded spatially localized significance maps of CP-driven contamination effects, which were used in downstream visualization and interpretation of artifact-prone regions.

## 2.8 Comparison with Voxel-wise Regression and Validation

To contextualize the advantages of our surface-based framework, we compared our results with a conventional voxel-wise regression approach. Specifically, we performed voxel-wise linear regressions at each voxel within the bilateral hippocampus (defined by the AAL2 atlas), modeling SUVR values using the same covariates and interaction terms as in our surface-based analysis (see Section 2.6). For comparison, we extracted voxels closest to the medial principal surface and visualized the corresponding significance maps for subtype 1.

As an external validation of our pipeline, we implemented our proposed workflow on ADNI amyloid-PET data (N=611; 129 CN, 412 MCI, 70 AD). Amyloid PET images were co-registered to the native T1-weighted MRI and normalized to the MNI152 template. SUVR was computed using cerebellar gray matter as the reference region for all tracers (PiB, AV45, FBB), and site/scanner effects harmonized via neuroCombat adjusting for age, sex, and diagnosis. Hippocampal geometry was defined from the AAL atlas; per subject, voxels with SUVR exceeding 1.1 formed an amyloid-positive mask that was then projected to the medial hippocampal surface. We report SuStaln staging, pointwise coverage of amyloid deposition on the hippocampal surface, covariate effects on amyloid SUVR, and stage-dependent effects on amyloid deposition thickness in Section 3.6. Complete details on the methods and results are provided in the Supplementary Material.

## 3 Results: Patterns of Hippocampal Tau Deposition Across Subtypes and Staging

In this section, we present key findings on where and how tau accumulates within the hippocampus, and how these patterns vary across diagnostic and demographic covariates. Together, these results demonstrate how surface-based geometric modeling enables high-resolution mapping of tau pathology and its covariate structure, revealing consistent spatial asymmetries and subtype-specific accumulation patterns across the hippocampal surface.

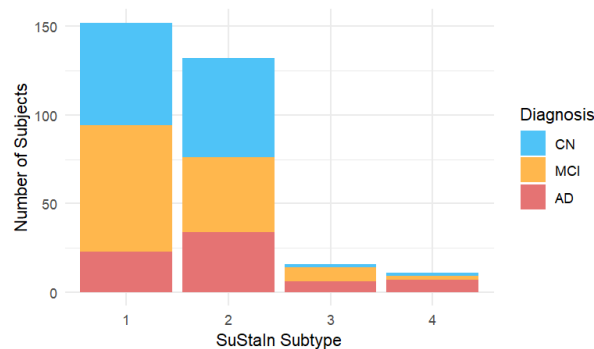
**SuStaln-Derived Subtypes and Disease Staging** Implementation of SuStraln yielded four distinct subtypes presented in Figure 3a–b, which correspond to previously described anatomical phenotypes (Vogel et al., 2021):

- **Subtype 1 (Limbic-dominant):** Tau accumulation begins in the medial temporal lobe (MTL)

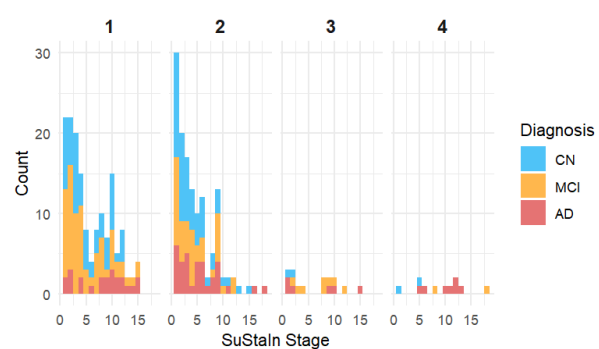
and spreads to the parietal and temporal cortices by Stage 11.

- **Subtype 2 (Posterior occipitotemporal phenotype):** Starts in the occipital cortex and proceeds anteriorly through the temporal lobe and MTL before reaching parietal and frontal areas.
- **Subtype 3 (Parietal-dominant, MTL-sparing phenotype):** Initiates in the parietal and temporal cortices, progressing to the frontal and occipital regions.
- **Subtype 4 (Left-temporal phenotype):** Characterized by early tau involvement in the left temporal cortex, followed by bilateral temporal and parietal spread.

The overall subtype distribution included 317 individuals assigned to subtype 0, and 152, 132, 16, and 11 assigned to subtypes 1 through 4, respectively. Subtype 0 corresponds to subjects with no suprathreshold regional tau deposition across regions, and is interpreted as a baseline group not exhibiting any trajectory of disease progression. This group includes a large proportion of CN participants and is consistent with a SuStain stage of 0. The diagnosis composition and stage distributions of the four non-zero subtypes are shown in Figure 3a–b. Subtypes 1 and 2 span a wide range of stages and include both CN and symptomatic individuals, while subtypes 3 and 4 are smaller and more skewed toward later stages and AD diagnosis. Given the limited sample size and reduced clinical variability of subtypes 3 and 4, all subsequent analyses focus on subtypes 1 and 2, which represent the dominant patterns of hippocampal tau accumulation in this cohort.



(a) Diagnosis within SuStain subtypes



(b) Stage across SuStain subtypes

Figure 3: Overview of SuStain-derived subtypes (a) Diagnosis composition (CN, MCI, AD) within each subtype, shown as a stacked bar plot. (b) Distribution of SuStain stages within each subtype, stratified by diagnosis. Subtype 1 and 2 are predominantly early-stage with a higher proportion of CN and MCI cases, while subtypes 3 and 4 are later-stage with more AD cases.

### 3.1 Pointwise Coverage of Tau Deposition on the Hippocampal Surface

To understand where suprathreshold tau deposition occurs across the hippocampus, we examined spatial coverage patterns using the logistic regression model described in Section 2.6. The number of scans in which each surface point was covered is visualized in Figure 4(a-b) for subtype 1 and subtype 2, respectively. In all plots, the surface is displayed with anterior at the bottom and posterior at the top, with the right hippocampus on the left and the left hippocampus on the right, matching a brain orientation facing the viewer. A consistent spatial trend is observed across both subtypes: the central region of the right hippocampus exhibits substantially higher coverage than any other region, including the corresponding location in the left hippocampus. This asymmetry suggests greater tau deposition in the lateral body of the right hippocampus across subjects and supports the robustness of the medial surface alignment.

We next evaluated how coverage patterns were modulated by covariates. Figures 4(c-f) display significance maps for the logistic regression coefficients associated with diagnosis and SuStAln stage in both subtypes. Diagnosis shows a significant and spatially distinct effect in subtype 2 (panel b), with widespread significant regions, including many points at  $p < 0.001$ . These regions are concentrated along the lateral surface of the mid and posterior hippocampus. In these areas, the estimated coefficients are consistently positive, indicating that more severe diagnosis is associated with an increased likelihood of suprathreshold tau signal. This pattern suggests that subtype 2 captures a progression-related accumulation process, particularly in the lateral posterior hippocampus. In subtype 1, diagnosis exhibits a weaker and more diffuse effect, with only scattered significance observed in the medial hippocampus, though the estimated coefficients remain positive.

SuStAln stage was also included in the model to account for variation along the disease progression axis. To reflect its ordinal nature (20 levels), stage was encoded as a second-order polynomial. Both the linear and quadratic components are shown in Figure 4 (e-h). Linear estimates were positive and broadly distributed in both subtypes, indicating that advancing stage increases the likelihood of suprathreshold tau signal. The two subtypes showed highly similar spatial patterns: in the right hippocampus, stage effects extended across the full surface, with slightly weaker signals in the central region of subtype 1. In the left hippocampus, significant effects were concentrated medially and anteriorly, with minimal lateral involvement. Subtype 1 showed slightly stronger effects in the mid-to-posterior medial region compared to subtype 2. Beyond these linear effects, second-order (quadratic) components revealed marked subtype differences. Subtype 1 exhibited widespread negative quadratic coefficients across most of the surface, except for a narrow band in the mid-posterior medial region, whereas subtype 2 showed no significant quadratic terms. These patterns suggest a plateauing of coverage expansion in later stages for subtype

1, consistent with a rapid early accumulation phase followed by deceleration—a biologically plausible trajectory for the limbic-dominant subtype, where tau deposition typically initiates early in the medial temporal lobe.

Age and sex were also included in the model. Age showed a small but significant negative effect in the anterior medial portion of the left hippocampus in subtype 1, suggesting higher tau signal among younger individuals, whereas subtype 2 showed no significant age or sex effects. Complete results are shown in Supplementary Figure S3.

### 3.2 Covariate Effects on Tau Deposition Intensity (SUVR)

We next evaluated the effects of age, diagnosis, and SuStaln stage on hippocampal tau SUVR, separately within each subtype. The significance maps are shown in Figure 5, and corresponding regression coefficient estimates are provided in Supplementary Figure S6. Age-related effects were observed in subtype 1, with significant regions localized to the mid-to-posterior lateral surface of the right hippocampus and the mid-lateral portion of the left hippocampus (Figure 5a). These areas exhibited positive regression coefficients (Supplementary Figure S6), indicating that older individuals within this subtype tend to show greater hippocampal tau SUVR. In contrast, subtype 2 showed no significant age effects (Figure 5b), suggesting a markedly different age–tau relationship. This divergence may reflect underlying differences in tau progression mechanisms, with the limbic subtype exhibiting greater sensitivity to age-related tau accumulation. Consistent with this interpretation, previous studies (Crutch et al., 2012) have reported that limbic-predominant subtypes tend to occur in older individuals with greater medial temporal vulnerability, whereas posterior variants such as PCA typically present earlier and display more uniform age distributions and reduced hippocampal involvement.

Diagnosis effects were also predominantly observed in subtype 1, with spatial distributions closely resembling the age-related patterns (Figure 5c). Significant regions were again localized to the right mid-to-posterior lateral surface and the left mid-lateral hippocampus. In subtype 2, the right hippocampus exhibited a similar pattern to subtype 1, while the left hippocampus showed a more spatially restricted cluster centered in the mid-region. Interestingly, the regression coefficients for diagnosis were negative in both subtypes (Supplementary Figure S6), a finding that may reflect limitations in the clinical diagnostic labeling process. This apparent inversion underscores the value of SuStaln stage as a more continuous and data-driven marker of disease progression, potentially more robust than categorical diagnosis for capturing spatial patterns of tau deposition.

Linear SuStaln stage effects showed strong and widespread significance in both subtypes (Figure 5e–f),

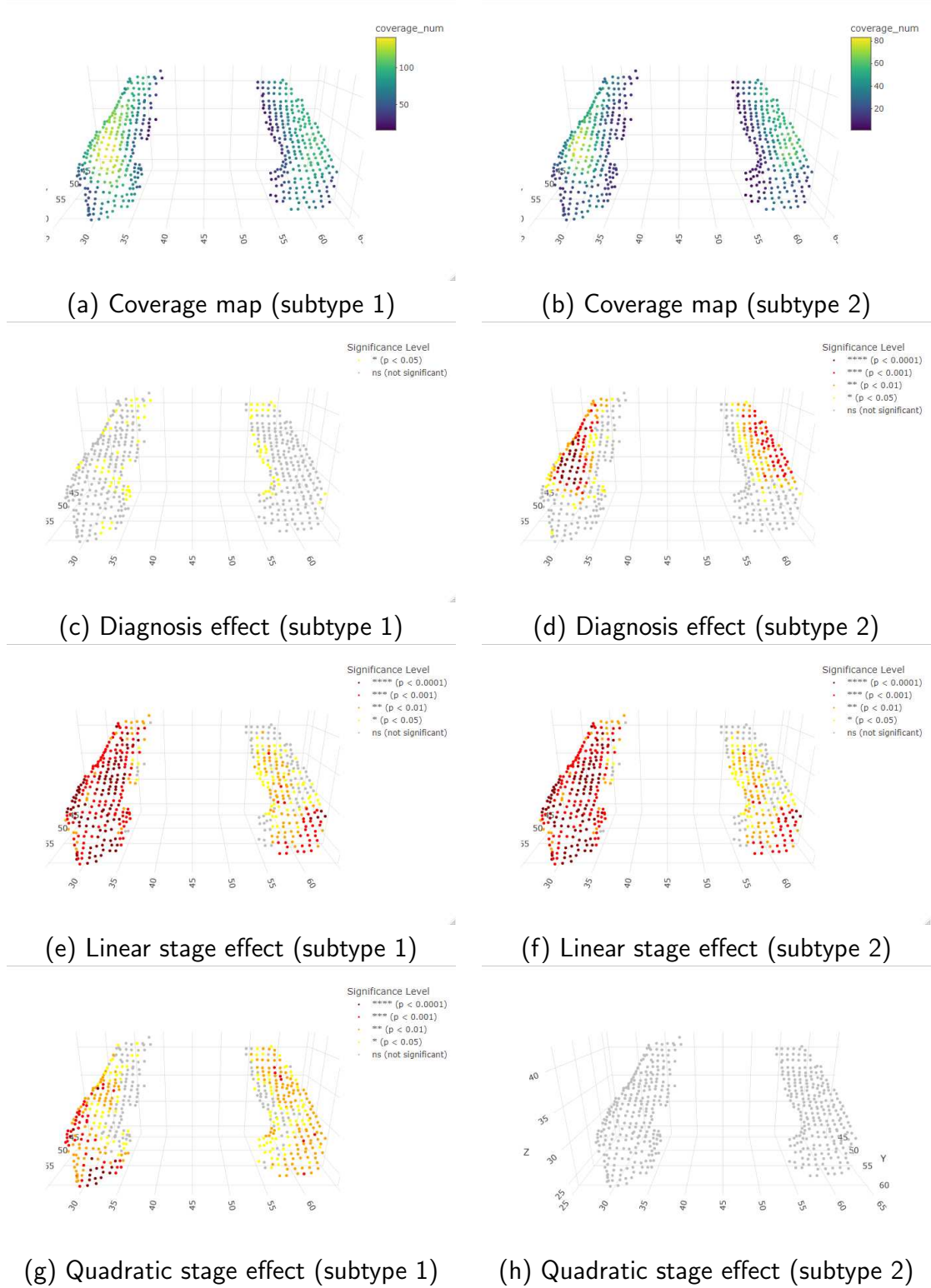


Figure 4: Coverage and significance maps for covariate effects on suprathreshold tau signal across the hippocampal surface. Panels (a-b) display the number of scans showing suprathreshold signal ( $SUVR > 2$ ) at each surface location for subtype 1 and subtype 2, respectively. Panels (c-d) show the significance of diagnosis effects on tau coverage, estimated using IPW-adjusted logistic regression. Panels (e-h) depict the significance of linear and quadratic SuStaln stage effects, where the “linear” and “quadratic” components correspond to the first two orthogonal polynomial terms.

with consistently positive regression coefficients across the hippocampal surface. The spatial patterns were highly similar between subtypes, with subtype 1 showing weaker effects in the left posterior hippocampus. Notably, anterior regions exhibited minimal significance in both subtypes, supporting a spatially constrained progression pattern that may reflect early-stage sparing of the anterior hippocampus. Beyond these broadly similar linear effects, the quadratic components revealed an opposite trend to that observed in coverage (Figure 5g–h). Subtype 2 exhibited significant positive quadratic effects in the right middle and left anterior hippocampus, whereas subtype 1 showed no such effects. This pattern suggests that in subtype 2, SUVR continues to increase even at later stages—possibly reflecting a slower but more persistent accumulation trajectory—while subtype 1 shows more stable, approximately linear intensity changes across progression.

Interaction analyses further confirmed these subtype-specific divergences. Significant age-by-subtype interactions were observed along a continuous band in the right posterior-to-mid hippocampus, with sparser yet spatially corresponding effects in the left hemisphere (Figure 7a). A spatially confined but significant linear stage-by-subtype interaction was also detected in the posterior portion of the left hippocampus (Figure 7b), indicating meaningful heterogeneity in SUVR progression patterns between subtypes.

The effect of sex was negligible in both subtypes, with only a few scattered regions showing weak association in subtype 2. Complete p-value and coefficient maps for sex are provided in Supplementary Figure S5.

### 3.3 Stage-Dependent Effects on Tau Deposition Thickness

To capture shape-level changes in tau pathology beyond intensity or coverage, we analyzed a geometric measure of deposition thickness based on projection distance. Specifically, we considered two complementary directional components: positive and negative projection distance, defined by projecting suprathreshold signal along opposite directions of the local surface normal from the medial principal surface. These features reflect signal expansion relative to hippocampal geometry, and together quantify bidirectional changes in local thickness centered on the surface. Covariate effects on thickness were estimated using IPW-adjusted linear regression. Age, sex, and diagnosis did not show significant effects in either projection direction across subtypes; full results are provided in Supplementary Figure S8. We therefore focus on the effects of SuStAln stage.

Linear stage effects were robust in both subtypes and across both projection directions (Figure 6a–d). In each subtype, the spatial pattern of significance was nearly identical between the positive and negative features, indicating that tau thickness increases occur symmetrically around the principal surface.

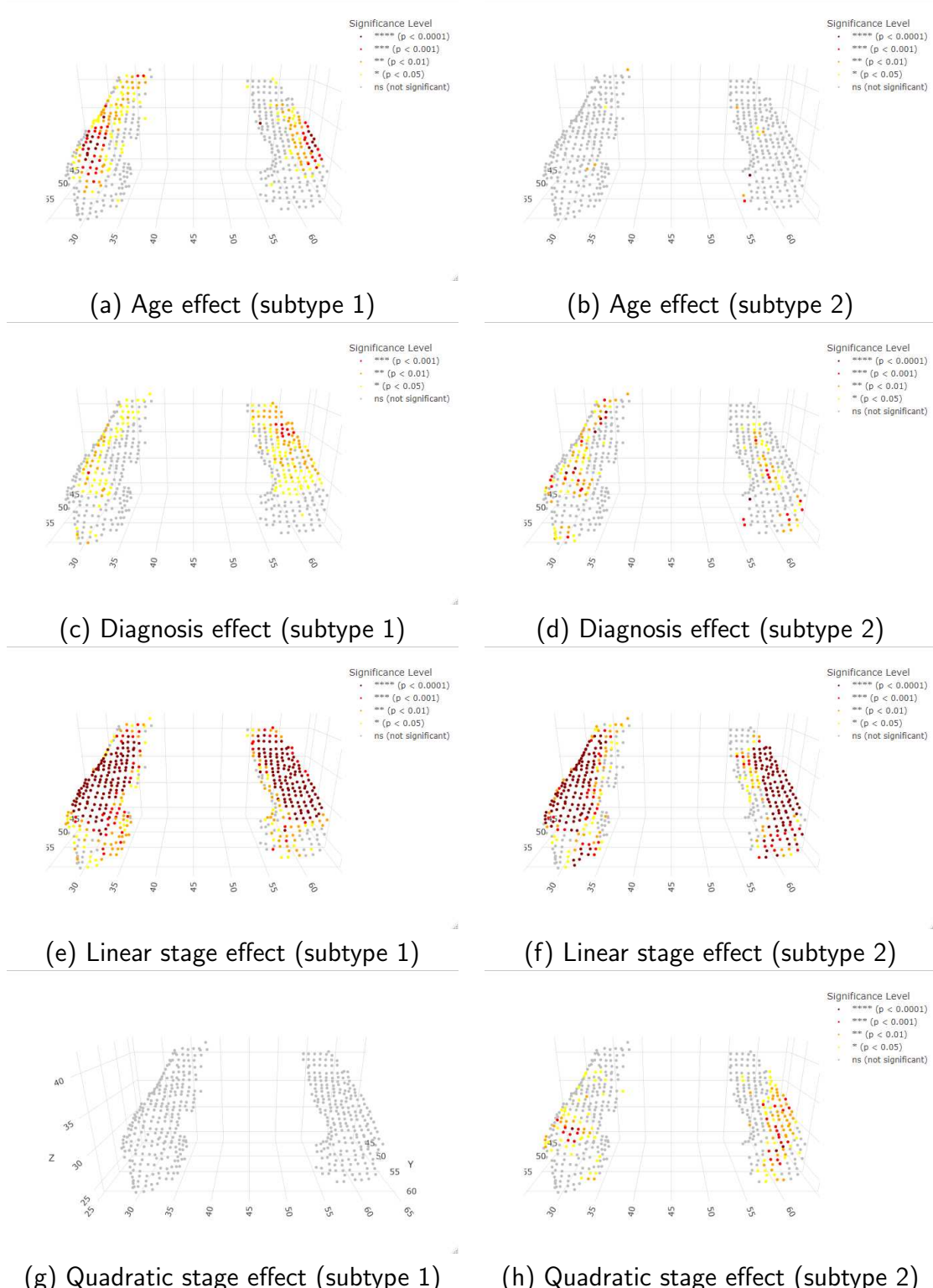


Figure 5: Significance maps of covariate effects on hippocampal tau SUVR. (a-b) Age-related effects show a small significant cluster in the middle lateral part of hippocampus of subtype 1. (c-d) Diagnosis-related effects are stronger in subtype 1, with multiple significant regions concentrated along the mid-to-posterior lateral surface. (e-h) SuStAln stage, linear effect with positive coefficients widespread in subtype 1 and 2, while quadratic effect with negative coefficients observed in subtype 2.

Subtype 1 showed a broader region with smaller p-values in the negative direction, particularly in the right hippocampus, where the spatial extent of significant vertices exceeded that of the left. Subtype 2, in contrast, showed similar significance levels across directions, but with spatial localization primarily to the lateral surface, while medial regions remained non-significant. These results reinforce the effectiveness of the principal surface representation in separating hippocampal geometry into spatially meaningful upper and lower regions, while also revealing asymmetric expansion rates across directions in subtype 1 and more uniform expansion in subtype 2.

Quadratic stage effects were only significant in subtype 1 and are visualized in Figure 6e-h. Both positive and negative features showed overlapping significant regions, and the corresponding regression coefficients were consistently negative (Supplementary Figure S10a-d), indicating a deceleration of thickness increase at later stages. Subtype 2 showed no significant quadratic effects, and those results are included in the supplementary material.

Interaction analyses yielded only sparse but spatially consistent covariate-by-subtype differences in thickness (Figure 7c-f). Most significant effects were localized near the central body of the hippocampus—regions known to exhibit greater morphological thickness and higher susceptibility to tau aggregation.

Taken together, these results highlight a consistent subtype divergence across all feature domains. The limbic subtype (subtype 1) displays early, aggressive expansion of tau signal in both coverage and thickness, followed by a deceleration phase—while the posterior subtype (subtype 2) exhibits slower but more persistent accumulation. Notably, while coverage and thickness capture spatial and shape-related changes, SUVR directly reflects signal intensity, and the reversal in quadratic effects between these modalities underscores the multidimensional nature of subtype-specific progression.

### 3.4 Spatial Patterns of Choroid Plexus Contamination

**Subject-Level Patterns of Contamination** To visualize spatial manifestations of CP contamination at the individual level, we present representative participants from each diagnostic group (CN, MCI, AD), arranged in order of increasing hippocampal tau burden (Supplementary Figure S14). Each row corresponds to one subject, with significance maps for both positive and negative contamination directions. Consistent with our hypothesis, CN and MCI participants — who show minimal hippocampal tau — exhibit strong **positive contamination**, where SUVR increases near the hippocampal surface adjacent to the CP. In contrast, AD participants show more pronounced **negative contamination**, suggesting that elevated hippocampal tau leads to signal mixing with adjacent non-tau regions, resulting in SUVR

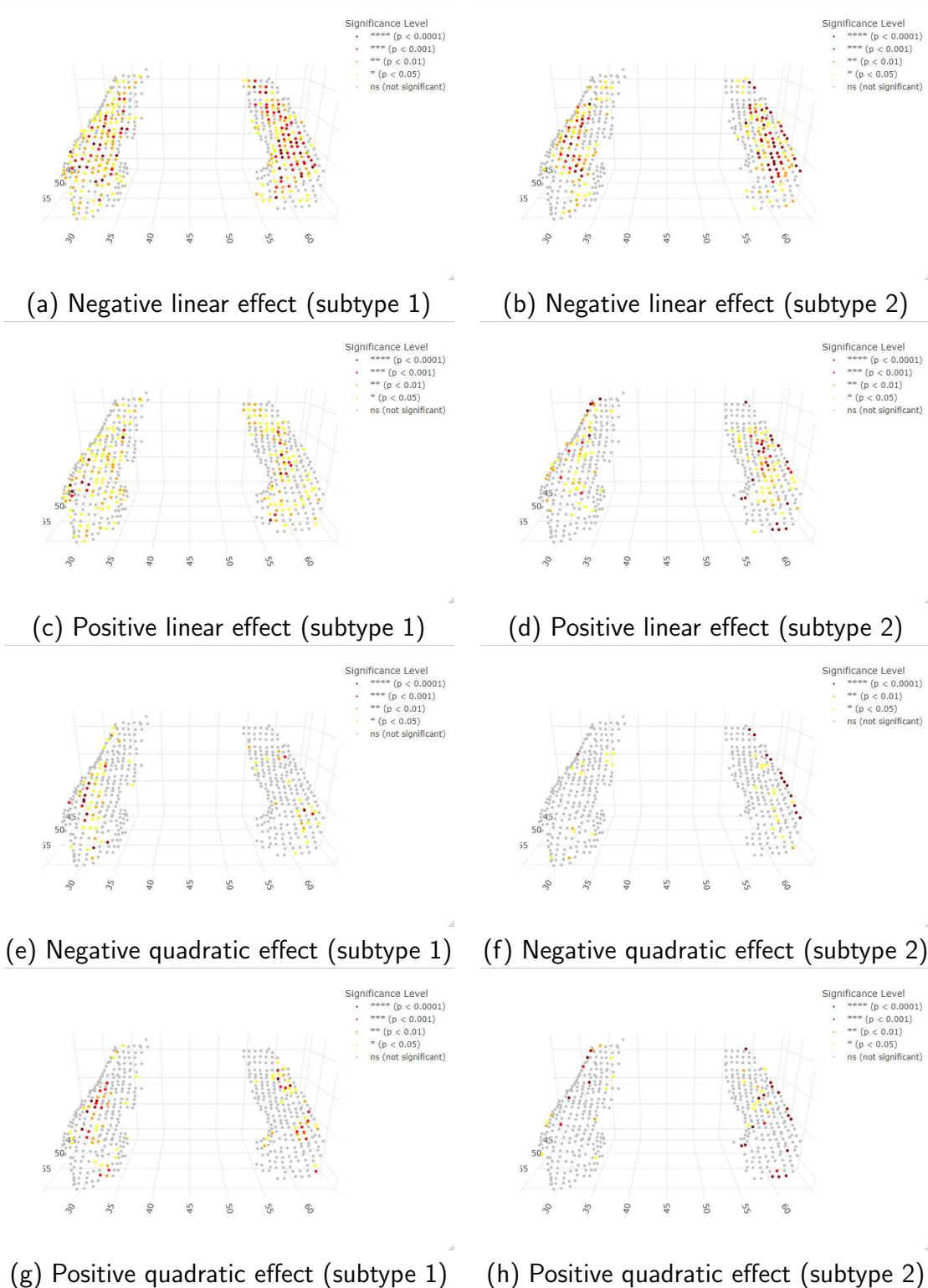


Figure 6: Significance maps of SuStAln stage effects on hippocampal tau deposition thickness, separated by subtype, projection direction, and polynomial term. Each panel shows results from an IPW-adjusted regression model fit within a specific subtype. Panels (a–d) correspond to linear stage effect for projection distances; (e–h) show quadratic stage effect for projection thickness. All maps display  $-\log_{10}(p)$  values thresholded at multiple significance levels after BH correction for multiple comparisons. Subtype labels are indicated in parentheses for consistency with other figures.

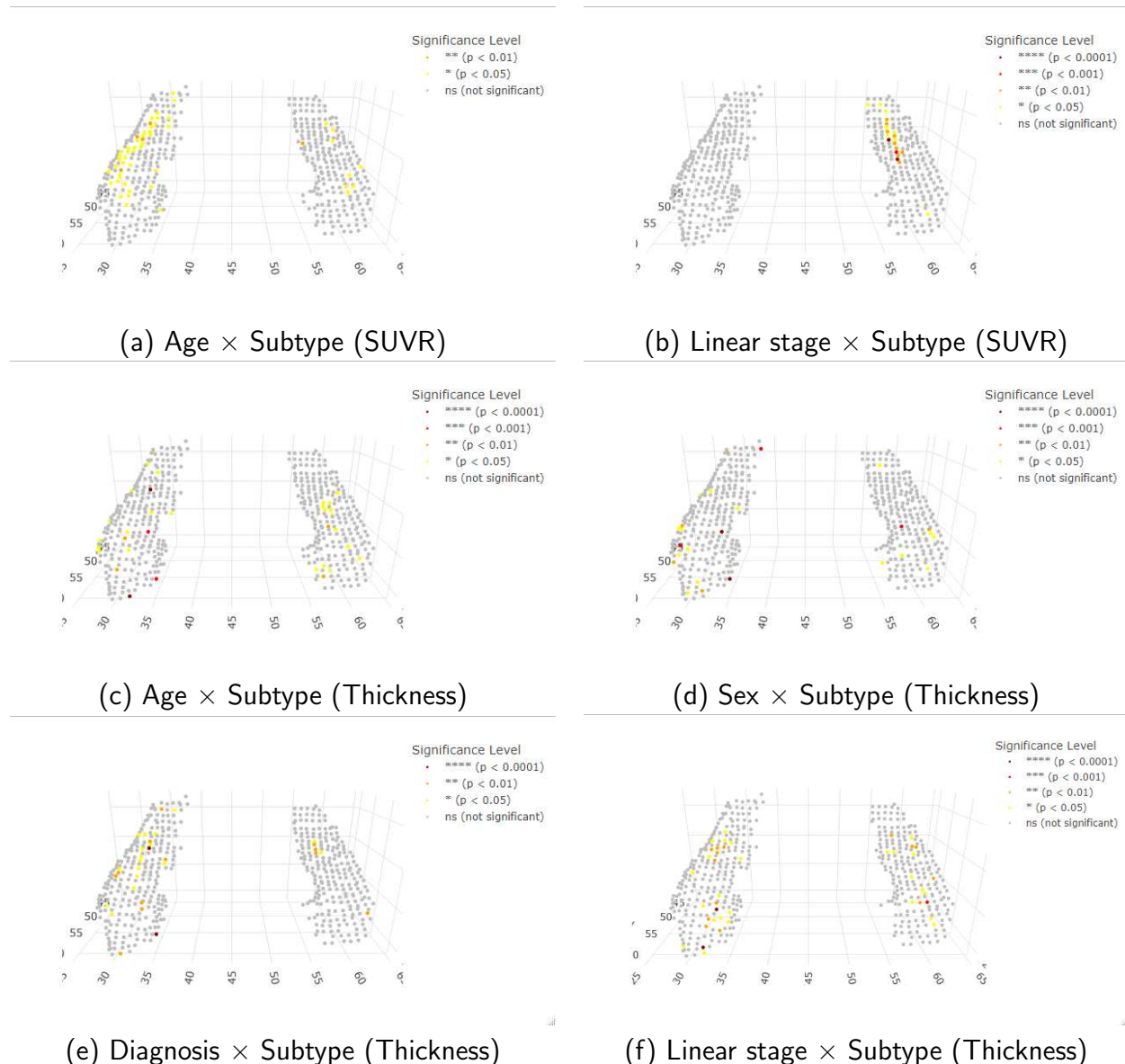


Figure 7: Significance maps for covariate-by-subtype interaction terms in the unified regression model. Each map displays surface regions where the effect of a covariate on tau deposition differs significantly between subtypes. (a) Significance of the age effect interaction on SUVR intensity; (b) Interaction significance for SuStaln stage (linear term) on SUVR intensity; (c) Interaction significance of age on negative projection thickness; (d) Interaction significance of sex on negative projection thickness; (e) Interaction significance of diagnosis on negative projection thickness; (f) Interaction significance of SuStaln stage (linear term) on negative projection thickness. All maps display  $-\log_{10}(p)$  values from IPW-adjusted regression models, with multiple significance levels indicated by color intensity. Benjamini–Hochberg correction was applied across all vertices to control for multiple comparisons.

underestimation.

**Group-Level Patterns of Contamination** Figure 8 shows group-level CP contamination patterns for the full cohort of 628 participants from ADNI derived from one-sample  $t$ -tests on  $\beta_1$  coefficients across individuals. Each panel presents significant contamination effects, separated by direction (positive vs. negative) and diagnostic group. In CN and MCI groups, where hippocampal tau signal is generally low, we observe widespread positive contamination (panels b and d). This aligns with the hypothesis that CP signal inflates SUVR when native tau is weak. In contrast, AD groups display prominent negative contamination in the central body of the hippocampus (panel e), with residual positive contamination in both anterior and posterior extremities (panel f). This spatial separation reflects the curved anatomical structure of the hippocampus, where CP contamination proximity varies along the anterior-posterior axis. These findings reinforce the directionality of CP contamination: weak tau in hippocampus  $\rightarrow$  upward bias (positive  $\beta_1$ ); strong tau in hippocampus  $\rightarrow$  downward bias (negative  $\beta_1$ ). Importantly, the contamination is not spatially uniform but follows systematic, geometry-driven patterns.

### 3.5 Stage-Wise Prediction of Hippocampal Tau Shape via Two-Stage Regression

Building upon pointwise regression analyses that quantified how age, sex, diagnosis, and disease stage influence tau deposition features across the hippocampal surface, we used the trained two-stage regression models to generate predicted hippocampal tau shapes across SuStAln stages. This predictive framework combines a logistic regression for tau coverage with stage-weighted linear models for intensity and deposition thickness, and allows for model-based simulation of tau progression patterns. To simulate a representative disease trajectory, we fixed the covariates at cohort-typical values: age was set to 75.5 (the overall sample mean), sex to male, and diagnosis to MCI, which was the most prevalent and evenly distributed diagnosis category across disease stages. Using these fixed covariates, we varied the SuStAln stage from 1 to 15 and applied the model to each previously selected principal surface point to predict the probability of tau coverage and the associated deposition geometry.

We performed this simulation separately for subtype 1 and subtype 2, using their respective pointwise models. Since the first-stage logistic regression is central to determining whether a point is covered by tau, we evaluated the accuracy of the logistic models via ROC analysis. The area under the curve (AUC) was 0.834 for subtype 1 and 0.875 for subtype 2 (Supplementary Figure S13). These values indicate strong discriminative ability of the logistic models in predicting pointwise tau presence from

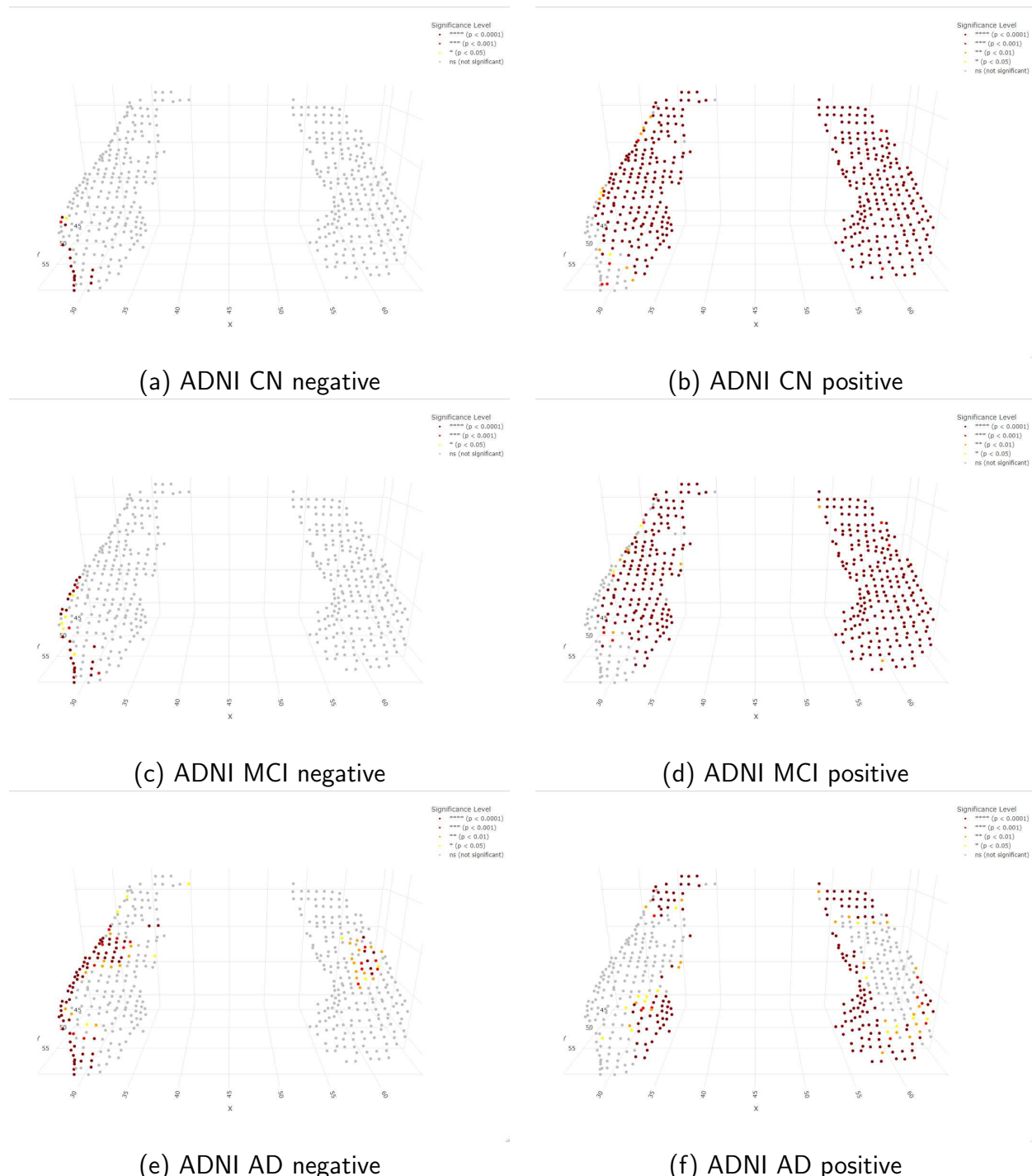


Figure 8: Group-level CP contamination significance maps from one-sample Right column: positive contamination (overestimation). Left column: negative contamination (underestimation). CN and MCI show widespread positive contamination, whereas the AD group exhibits central negative contamination with residual anterior/posterior positivity.

subject-level covariates. Based on Youden's index (Youden, 1950), we selected the optimal predicted probability threshold for tau coverage—0.498 for subtype 1 and 0.254 for subtype 2—and applied these thresholds to filter predicted coverage points when reconstructing tau deposition shapes.

Figure 9 illustrates the predicted tau deposition shapes for subtype 1 and subtype 2 at SuStaln stages 1, 4, 7, and 10. For subtype 1, the results demonstrate a smooth and biologically plausible progression of tau pathology across the hippocampal surface. Over-threshold tau accumulation ( $SUVR > 2$ ) emerges initially in the middle portion of the hippocampus at stage 1, and progressively extends both anteriorly and posteriorly along the longitudinal axis, as well as medially and laterally across the medial surface. This spatial expansion is accompanied by a gradual increase in predicted deposition thickness. These patterns indicate that high-intensity tau signal does not appear diffusely from the outset, but rather follows a structured, stage-wise trajectory of propagation within the hippocampus.

For subtype 2, tau deposition exhibits an earlier onset in the posterior hippocampus, consistent with the posterior progression pattern identified by whole-brain SuStaln modeling. Although the SuStaln stages were derived from global tau patterns, the predicted spatial expansion within the hippocampus aligns with the subtype-specific whole-brain trajectory. Similar to subtype 1, tau deposition in subtype 2 extends from initial focal regions toward anterior, posterior, and lateral areas, with increasing thickness and eventual involvement of the entire hippocampus. Compared to empirical averages—which are particularly unstable in late stages due to limited sample size—these model-based predictions provide a biologically plausible visualization of disease progression.

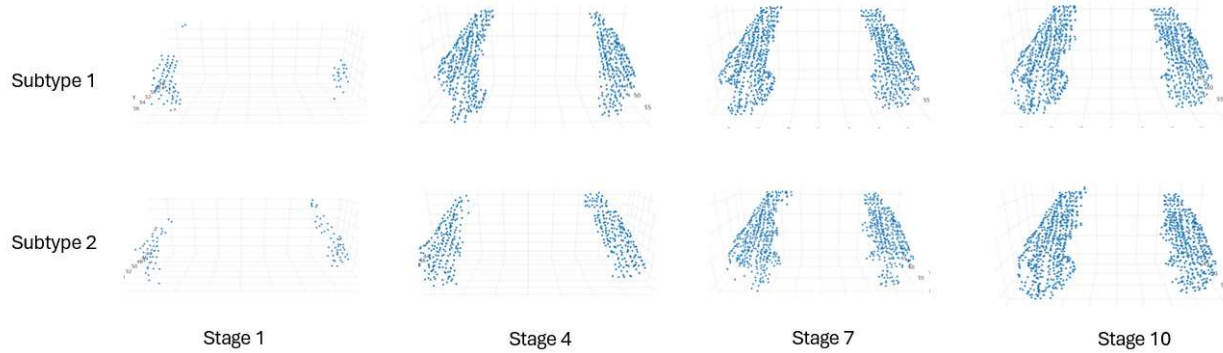


Figure 9: Model-based prediction of tau deposition shapes across SuStaln stages using two-stage regression. The first row shows predicted hippocampal tau deposition shapes for subtype 1 at SuStaln stages 1, 4, 7, and 10 (left to right). The second row shows corresponding predictions for subtype 2. Predictions were generated by fixing covariates (Age = 75.5, Sex = Male, Diagnosis = MCI) and varying stage input from 1 to 10. Each shape represents the reconstructed hippocampal surface based on predicted pointwise tau coverage and deposition thickness.

### 3.6 Comparison with Voxel-wise Regression and Validation

When comparing our results with that of running voxel-wise regression analyses, several key differences emerged. First, for age and diagnosis effects (Supplementary Figure S12 vs. Figure 5), our model yielded broader regions of significant voxels in both hippocampi. This is likely due to the dimensionality reduction achieved by medial surface projection, which reduced the number of statistical tests and alleviated the severity of multiple comparison correction, thereby increasing power. The advantage became even more apparent for the linear stage effect: voxelwise models failed to identify any significant points near the medial boundary, where coverage was sparse, whereas our model detected extensive significance in both hemispheres. This suggests that our method is more robust in regions with limited suprathreshold signal, where voxel-wise methods suffer from reduced sample size and inflated variance. In contrast, voxel-wise regression yielded isolated significance clusters in unexpected anatomical regions, such as anterior boundary voxels in the right hippocampus for the quadratic stage effect (Supplementary Figure S12d), likely reflecting spurious results due to noise or alignment error. Our method, in comparison, did not produce such isolated clusters, reflecting its robustness and geometric regularization.

We replicated the hippocampal projection pipeline on ADNI MRI co-registered amyloid-PET using a fixed suprathreshold mask ( $SUVR \geq 1.1$ ) and SuStAln staging (encoded with linear/quadratic terms), yielding one no-signal group (subtype 0;  $n = 312$ ) and four amyloid-positive subtypes ( $n = 101, 98, 88, 12$ ). Subtypes are analysis-specific and not mapped to canonical tau phenotypes. Given subtype 4's small, clinically skewed sample, we limited analyses to subtypes 1–3. Coverage maps show focal, right-lateral hotspots in the posterior/central body across subtypes. Linear stage shows widespread significance in subtypes 1 and 3 and only small clusters in subtype 2. Quadratic stage effects are negligible. Intensity models (SUVR) show no age effects. Diagnosis is significant only in localized regions in subtype 3 (right medial surface). Linear stage effects are widespread in subtypes 1 and 3 and small/confined in subtype 2. Quadratic stage effects are negligible in subtypes 3, with only localized regions in subtypes 1 and 2. Quantifying amyloid deposition thickness via projection distance metric showed that linear stage effects are prominent in subtype 3 across both projection directions, subtype 2 shows only small clusters. Overall, amyloid results indicate low, focal right-lateral hippocampal burden with consistent linear stage effects, supporting pipeline robustness. Details and figures are provided in the Supplementary Materials.

## 4 Discussion

In this study, we proposed a surface-based framework for high-resolution modeling of hippocampal tau deposition, integrating spatial coverage, SUVR intensity, and projection-based thickness features onto a medial principal surface. Using pre-defined SuStAln subtypes and progression stages, we investigated how tau accumulation varies across subtypes within the hippocampus, quantifying both spatial distributions and covariate effects. Our analyses revealed subtype-specific trajectories of tau pathology in this region, characterized by divergent nonlinear stage effects, differential covariate associations, and anatomically consistent signal patterns. These results demonstrate the utility of our framework for capturing biologically meaningful heterogeneity in regional tau deposition. A key strength of our framework lies in its ability to represent tau pathology along multiple complementary dimensions while preserving spatial specificity. By projecting tau features onto a shared medial principal surface, we achieve geometric alignment across individuals and reduce data dimensionality, enabling localized regression with greatly reduced multiple comparison burden compared to voxelwise analysis. Unlike traditional ROI approaches, our method retains fine-grained spatial resolution, and the principal surface representation preserves sufficient geometric structure to reconstruct full hippocampal shapes when needed. This framework also facilitates a clear separation between shape-derived features (coverage and thickness) and signal intensity (SUVR), allowing distinct patterns to emerge across feature domains.

From a methodological perspective, our framework integrates anatomical structure via a medial manifold representation and restricts analysis to biologically meaningful suprathreshold signal—excluding low-SUVR regions that are unlikely to reflect true tau deposition. This over-threshold constraint provides greater biological interpretability than regional SUVR averages and ensures that regression targets reflect true signal distribution rather than background variability. While the optimal threshold remains an open question, our approach provides a powerful and interpretable model for investigating spatial tau accumulation patterns. These results on comparison of our proposed method with voxel-wise regression demonstrate that our surface-based approach offers improved statistical power, anatomical alignment, and biological interpretability relative to voxel-wise regression, making it a preferable choice for analyzing sparse, spatially structured PET data.

Our surface-based representation of hippocampal tau deposition allows decoupling structural features into three interpretable components: suprathreshold coverage, local thickness, and signal intensity. To model covariate effects on these features, we employed a two-stage regression strategy with IPW, correcting for selection bias induced by signal-dependent inclusion. This IPW-adjusted method was especially effective in improving the stability of SUVR-based regression. As shown in Supplementary Figure S7, IPW correction revealed diagnosis-related effects in subtype 2 that were otherwise obscured, bringing

them into spatial agreement with the more robust patterns observed in subtype 1. Similar gains were observed for age effects and across thickness and coverage models. These improvements highlight the utility of IPW-enhanced modeling for detecting spatially nuanced effects in sparsely expressed tau signals.

Importantly, we found that the covariate modeling results were robust to variations in the threshold used to define tau positivity. Although we adopted a fixed SUVR threshold of 2.0 in our analysis, alternative thresholds (e.g., 1.8, 2.2) produced qualitatively similar regression coefficients despite changes in surface coverage patterns. The robustness to threshold choice means that downstream modeling results remain stable across reasonable cutoffs, allowing flexible yet reliable use in practice. In future applications, e.g. in other brain regions, the SUVR threshold can be redefined as a task-specific, tunable parameter.

Our results reveal consistent spatial and temporal differences in tau accumulation across SuStain-derived subtypes. The limbic-predominant subtype (subtype 1) exhibited early and widespread tau deposition in the medial temporal lobe, followed by a plateau in both spatial coverage and projection-based thickness—evidenced by strong negative quadratic effects of SuStain stage. In contrast, the posterior subtype (subtype 2) showed minimal nonlinearity in these shape-related features, but exhibited accelerating SUVR increases in posterior and lateral hippocampal regions at later stages. These divergent trajectories suggest that subtype 1 follows a rapid early accumulation with subsequent saturation, while subtype 2 progresses more gradually but with sustained expansion in signal intensity and anatomical extent.

Beyond staging effects, we also observed subtype-specific associations with age. Only subtype 1 showed significant age-related increases in hippocampal SUVR, reinforcing the idea that tau intensity in limbic-predominant disease is more tightly coupled to aging processes. In contrast, subtype 2—consistent with posterior variants such as PCA—appeared largely age-independent, with a narrower age range and reduced hippocampal involvement. These findings are aligned with prior reports (Crutch et al., 2012) and demonstrate how our surface-based, subtype-aware analysis refines existing knowledge by linking spatially resolved tau phenotypes with demographic and biological heterogeneity.

In addition to subtype-level differences in overall signal and shape metrics, our predictive modeling revealed that tau deposition within the hippocampus also follows a subtype-specific spatial expansion pattern. Using the two-stage regression models, we simulated tau progression across disease stages under fixed covariates, and found that in subtype 1, tau consistently originated in the middle segment of the hippocampus and extended along both anterior-posterior and medial-lateral axes, accompanied by increasing deposition thickness. Subtype 2, by contrast, exhibited an initial signal peak in the posterior hippocampus, aligning with its broader posterior cortical phenotype. These results suggest that even within a region traditionally regarded as the starting point of tau accumulation, the spatial dynamics of pathology may differ depending on subtype. The observation that tau does not emerge diffusely, but

instead follows a systematic expansion trajectory, reinforces the biological coherence of SuStAln-derived staging, and provides a fine-grained view of intra-hippocampal propagation that may inform future models of tau spread.

Beyond regression-based phenotyping, our framework also supports additional analytical capabilities. We demonstrated that directional patterns of SUVR signal on the principal surface can be leveraged to detect potential contamination from adjacent structures, such as the choroid plexus. Specifically, asymmetric anterior or inferior signal distributions—misaligned with expected hippocampal anatomy—served as indicators of spill-in, highlighting the utility of this approach for identifying imaging artifacts within surface space. Such functionality could be extended into automated quality control pipelines, particularly in studies comparing PET signal across populations or imaging centers.

The generalizability of our approach opens avenues for future work. While this study focused on the hippocampus in AD, the framework is readily extensible to other brain regions and disease models. For example, projection-based tau thickness could be adapted for neocortical surfaces, or applied to other tracers such as amyloid PET or FDG. The regression modeling scheme can accommodate additional biomarkers or longitudinal trajectories, offering a flexible platform for capturing disease heterogeneity. We anticipate that this framework can contribute to more precise biomarker analysis in both clinical and research settings, especially in subtype-aware modeling of neurodegeneration.

## Data and Code Availability

**ADNI data set** Data used in the preparation of this article were obtained from the Alzheimer’s Disease Neuroimaging Initiative (ADNI) database (<http://adni.loni.usc.edu>).

**Code Availability** All code for preprocessing, geometric modeling, regression analysis, and figure generation is openly available at <https://github.com/LaoWang-123/PS-analysis>. The repository includes a general pipeline, scripts for reproducing the analyses and figures in this paper, and supporting utility functions. Due to ADNI data use restrictions, no subject-level imaging or demographic data are included. Researchers can request access to the raw data directly from ADNI at <http://adni.loni.usc.edu>.

## Author Contributions

## Funding

This research was supported by the National Institutes of Aging grant 5R01AG075511. The content is solely the responsibility of the authors and does not necessarily represent the official views of the NIH.

## Declaration of Competing Interests

The authors declare no competing interests.

## Acknowledgements

Data collection and sharing for this project was funded by the Alzheimer's Disease Neuroimaging Initiative (ADNI) (National Institutes of Health Grant U01 AG024904) and DOD ADNI (Department of Defense award number W81XWH-12-2-0012). ADNI is funded by the National Institute on Aging, the National Institute of Biomedical Imaging and Bioengineering, and through generous contributions from the following: AbbVie, Alzheimer's Association; Alzheimer's Drug Discovery Foundation; Araclon Biotech; BioClinica, Inc.; Biogen; Bristol-Myers Squibb Company; CereSpir, Inc.; Cogstate; Eisai Inc.; Elan Pharmaceuticals, Inc.; Eli Lilly and Company; Eurolmmun; F. Hoffmann-La Roche Ltd and its affiliated company Genentech, Inc.; Fujirebio; GE Healthcare; IXICO Ltd.; Janssen Alzheimer Immunotherapy Research & Development, LLC.; Johnson & Johnson Pharmaceutical Research & Development LLC.; Lumosity; Lundbeck; Merck & Co., Inc.; Meso Scale Diagnostics, LLC.; NeuroRx Research; Neurotrack Technologies; Novartis Pharmaceuticals Corporation; Pfizer Inc.; Piramal Imaging; Servier; Takeda Pharmaceutical Company; and Transition Therapeutics. The Canadian Institutes of Health Research is providing funds to support ADNI clinical sites in Canada. Private sector contributions are facilitated by the Foundation for the National Institutes of Health ([www.fnih.org](http://www.fnih.org)). The grantee organization is the Northern California Institute for Research and Education, and the study is coordinated by the Alzheimer's Therapeutic Research Institute at the University of Southern California. ADNI data are disseminated by the Laboratory for Neuro Imaging at the University of Southern California.

## References

Aksman, L. M., Wijeratne, P. A., Oxtoby, N. P., et al. (2021). Pysustain: A python implementation of the subtype and stage inference algorithm. *SoftwareX*, 16, 100811. <https://doi.org/https://doi.org/10.1016/j.softx.2021.100811>

Benjamini, Y., & Hochberg, Y. (1995). Controlling the false discovery rate: A practical and powerful approach to multiple testing. *Journal of the Royal Statistical Society: Series B (Methodological)*, 57(1), 289–300. <https://doi.org/https://doi.org/10.1111/j.2517-6161.1995.tb02031.x>

Better, M. A. (2023). Alzheimer's disease facts and figures. *Alzheimers Dement*, 19(4), 1598–1695.

Blum, H. (1967). A transformation for extracting new descriptors of shape (W. Wathen-Dunn, Ed.) [Pages: 362-380 Publication Title: Models for the Perception of Speech and Visual Form Place: Cambridge, MA].

Bouix, S., Pruessner, J. C., Louis Collins, D., et al. (2003). Flux Invariants for Shape. *2013 IEEE Conference on Computer Vision and Pattern Recognition*, 2, 835. <https://doi.org/10.1109/CVPR.2003.1211439>

Bouix, S., Pruessner, J. C., Louis Collins, D., et al. (2005). Hippocampal shape analysis using medial surfaces. *NeuroImage*, 25(4), 1077–1089. <https://doi.org/https://doi.org/10.1016/j.neuroimage.2004.12.051>

Chen, S.-D., Lu, J.-Y., et al. (2021). Staging tau pathology with tau pet in alzheimer's disease: A longitudinal study. *Translational Psychiatry*, 11(1), 483. <https://doi.org/10.1038/s41398-021-01602-5>

Cleveland, W. S., Grosse, E., & Shyu, W. M. (1992). Local regression models. In J. Chambers & T. Hastie (Eds.), *Statistical models in s*. Wadsworth & Brooks/Cole.

Crutch, S. J., Lehmann, M., Schott, J. M., et al. (2012). Posterior cortical atrophy. *The Lancet Neurology*, 11(2), 170–178. [https://doi.org/https://doi.org/10.1016/S1474-4422\(11\)70289-7](https://doi.org/https://doi.org/10.1016/S1474-4422(11)70289-7)

Eisma, J. J., McKnight, C. D., Hett, K., et al. (2024). Deep learning segmentation of the choroid plexus from structural magnetic resonance imaging (mri): Validation and normative ranges across the adult lifespan. *Fluids and Barriers of the CNS*, 21(1), 21. <https://doi.org/10.1186/s12987-024-00525-9>

Fortin, J.-P. (2024). *Neurocombat: Harmonization of multi-site imaging data with combat*.

Hernan, M. A. (2024). *Causal inference: What if*. Taylor & Francis.

Joseph, A. T. (2004). Understanding the standardized uptake value, its methods, and implications for usage. *Journal of Nuclear Medicine*, 45(9), 1431. <http://jnm.snmjournals.org/content/45/9/1431.abstract>

La Joie, R., Visani, A. V., Baker, S. L., et al. (2020). Prospective longitudinal atrophy in alzheimer's disease correlates with the intensity and topography of baseline tau-pet. *Sci Transl Med*, 12(524). <https://doi.org/10.1126/scitranslmed.aau5732>

Lah, J. J., Tian, G., Risk, B. B., et al. (2024). Lower prevalence of asymptomatic alzheimer's disease among healthy african americans. *Annals of Neurology*, 96(3), 463–475. <https://doi.org/10.1002/ana.26960>

Ossenkoppele, R., Lyoo, C. H., Sudre, C. H., et al. (2020). Distinct tau pet patterns in atrophy-defined subtypes of alzheimer's disease. *Alzheimers Dement*, 16(2), 335–344. <https://doi.org/10.1016/j.jalz.2019.08.201>

Pawlik, D., Leuzy, A., Strandberg, O., & Smith, R. (2020). Compensating for choroid plexus based off-target signal in the hippocampus using (18)f-flortaucipir pet. *Neuroimage*, 221, 117193. <https://doi.org/10.1016/j.neuroimage.2020.117193>

Pemberton, H. G., Collij, L. E., Heeman, F., et al. (2022). Quantification of amyloid pet for future clinical use: A state-of-the-art review. *European Journal of Nuclear Medicine and Molecular Imaging*, 49(10), 3508–3528. <https://doi.org/10.1007/s00259-022-05784-y>

Petersen, R. C., Aisen, P. S., Beckett, L. A., et al. (2010). Alzheimer's disease neuroimaging initiative (adni): Clinical characterization. *Neurology*, 74(3), 201–9. <https://doi.org/10.1212/WNL.0b013e3181cb3e25>

Rolls, E. T., Joliot, M., & Tzourio-Mazoyer, N. (2015). Implementation of a new parcellation of the orbitofrontal cortex in the automated anatomical labeling atlas. *NeuroImage*, 122, 1–5. <https://doi.org/10.1016/j.neuroimage.2015.07.075>

Siddiqi, K., Bouix, S., Tannenbaum, A., et al. (2002). Hamilton-jacobi skeletons. *International Journal of Computer Vision*, 48(3), 215–231. <https://doi.org/10.1023/A:1016376116653>

Theriault, J., Pascoal, T. A., Lussier, F. Z., et al. (2022). Biomarker modeling of alzheimer's disease using pet-based braak staging. *Nature Aging*, 2(6), 526–535. <https://doi.org/10.1038/s43587-022-00204-0>

Vogel, J. W., Young, A. L., Oxtoby, N. P., et al. (2021). Four distinct trajectories of tau deposition identified in alzheimer's disease. *Nature Medicine*, 27(5), 871–881. <https://doi.org/10.1038/s41591-021-01309-6>

Waragai, M., Okamura, N., Furukawa, K., et al. (2009). Comparison study of amyloid pet and voxel-based morphometry analysis in mild cognitive impairment and alzheimer's disease. *Journal of the neurological sciences*, 285(1-2), 100–108.

Weber, C. J., Carrillo, M. C., Jagust, W., et al. (2021). The worldwide alzheimer's disease neuroimaging initiative: Adni-3 updates and global perspectives. *Alzheimer's & Dementia: Translational Re-*

search & Clinical Interventions, 7(1), e12226. <https://doi.org/https://doi.org/10.1002/trc2.12226>

Wolters, E. E., Ossenkoppele, R., Golla, S. S., Verfaillie, S. C., Timmers, T., Visser, D., Tuncel, H., Coomans, E. M., Windhorst, A. D., Scheltens, P., van der Flier, W. M., Boellaard, R., & van Berckel, B. N. (2020). Hippocampal [(18)f]flortaucipir bp(nd) corrected for possible spill-in of the choroid plexus retains strong clinico-pathological relationships. *Neuroimage Clin*, 25, 102113. <https://doi.org/10.1016/j.nicl.2019.102113>

Wood, S., N., Pya, & S"afken, B. (2016). Smoothing parameter and model selection for general smooth models (with discussion). *Journal of the American Statistical Association*, 111, 1548–1575.

Youden, W. J. (1950). Index for rating diagnostic tests [Youden, w j Journal Article United States 1950/01/01 Cancer. 1950 Jan;3(1):32-5. doi: 10.1002/1097-0142(1950)3:1<32::aid-cncr2820030106>3.0.co;2-3]. *Cancer*, 3(1), 32–5. [https://doi.org/10.1002/1097-0142\(1950\)3:1<32::aid-cncr2820030106>3.0.co;2-3](https://doi.org/10.1002/1097-0142(1950)3:1<32::aid-cncr2820030106>3.0.co;2-3)

Young, A. L., Marinescu, R. V., Oxtoby, N. P., et al. (2018). Uncovering the heterogeneity and temporal complexity of neurodegenerative diseases with subtype and stage inference. *Nature Communications*, 9(1), 4273. <https://doi.org/10.1038/s41467-018-05892-0>

Yue, C., Zipunnikov, V., Bazin, P. L., et al. (2016). Parametrization of white matter manifold-like structures using principal surfaces. *J Am Stat Assoc*, 111(515), 1050–1060. <https://doi.org/10.1080/01621459.2016.1164050>

# Supplementary Figures

December 3, 2025

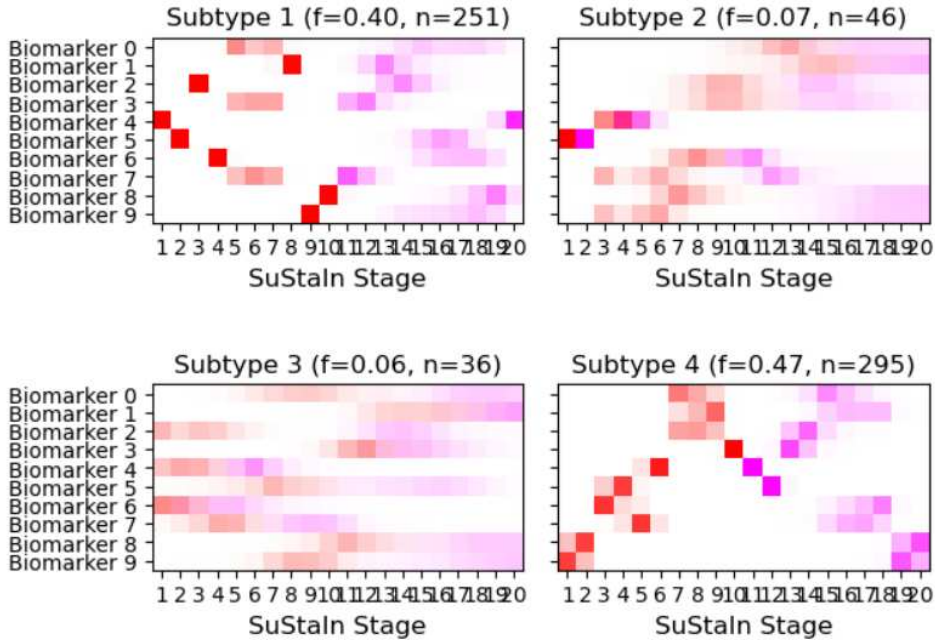


Figure S1: SuStaIn output matched with PVD plot

## 1 Directional consistency validation

### 1.1 Principal Surface Selection

To ensure that the principal surface (PS) provides an accurate and stable representation of tau deposition without overfitting, we evaluate its smoothness and geometric consistency using Gaussian curvature ( $K_i$ ). High curvature regions indicate potential overfitting, where the surface captures noise rather than meaningful structural variations. To mitigate this, we apply curvature-based filtering to prevent self-intersections and excessive flexibility in the PS fitting process, ensuring a stable yet representative surface.

Gaussian curvature is computed at each surface point  $\mathbf{q}_i = (x_i, y_i, z_i) = f(t_{1i}, t_{2i})$  using the first and second fundamental forms:

$$K_i = \frac{\mathbf{L}_i \mathbf{N}_i - \mathbf{M}_i^2}{\mathbf{E}_i \mathbf{G}_i - \mathbf{F}_i^2}.$$

where  $\mathbf{E}_i, \mathbf{F}_i, \mathbf{G}_i$  define local metric properties:

$$\mathbf{E}_i = \left\| \frac{\partial f}{\partial t_{1i}} \right\|^2, \quad \mathbf{F}_i = \frac{\partial f}{\partial t_{1i}} \cdot \frac{\partial f}{\partial t_{2i}}, \quad \mathbf{G}_i = \left\| \frac{\partial f}{\partial t_{2i}} \right\|^2,$$

and  $\mathbf{L}_i, \mathbf{M}_i, \mathbf{N}_i$  capture curvature variations:

$$\mathbf{L}_i = \mathcal{N}_i \cdot \frac{\partial^2 f}{\partial t_{1i}^2}, \quad \mathbf{M}_i = \mathcal{N}_i \cdot \frac{\partial^2 f}{\partial t_{1i} \partial t_{2i}}, \quad \mathbf{N}_i = \mathcal{N}_i \cdot \frac{\partial^2 f}{\partial t_{2i}^2}.$$

The unit normal vector  $\mathcal{N}_i$  at each point is computed as the cross product of the tangent vectors:

$$\mathcal{N}_i = \frac{\partial f}{\partial t_{1i}} \times \frac{\partial f}{\partial t_{2i}}.$$

To ensure numerical stability, derivatives are approximated using finite differences:

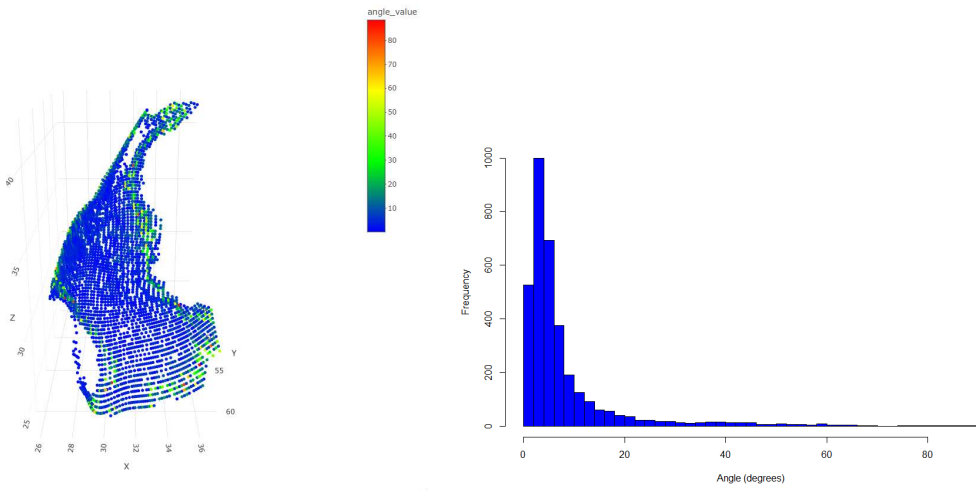
$$\frac{\partial f}{\partial t_{1i}} \approx \frac{f(t_{1i} + h, t_{2i}) - f(t_{1i} - h, t_{2i})}{2h},$$

$$\frac{\partial^2 f}{\partial t_{1i} \partial t_{2i}} \approx \frac{f(t_{1i} + h, t_{2i} + h) - f(t_{1i} + h, t_{2i} - h) - f(t_{1i} - h, t_{2i} + h) + f(t_{1i} - h, t_{2i} - h)}{4h^2}.$$

By analyzing the distribution of curvature values, we discard PS candidates with excessive local curvature that could lead to artifacts. The final selected surface balances smoothness and structural representation, ensuring a robust framework for subsequent tau deposition analysis.

## 1.2 Projection Vectors Difference

This representation assumes that the intrinsic normal vectors of the PS are well aligned with the projection directions from hippocampal boundaries. That is, when projecting a voxel from the boundary onto the PS (for distance computation or SUVR interpolation), the resulting vector should approximate the PS normal at the target point. While this holds in most regions, local misalignment may occur in areas of high curvature due to numerical approximation of normals (via finite differences) or the shortest-path projection strategy. The misalignment of two projection vectors can be found in Supplementary Figure S2.



(a) 3D Angle Distribution Map

(b) Angle Distribution Histogram

Figure S2: Directional consistency validation (a) Spatial map of angular differences between projection and normal vectors, showing localized misalignment. (b) Histogram of angle deviations confirms strong directional consistency across surface points.

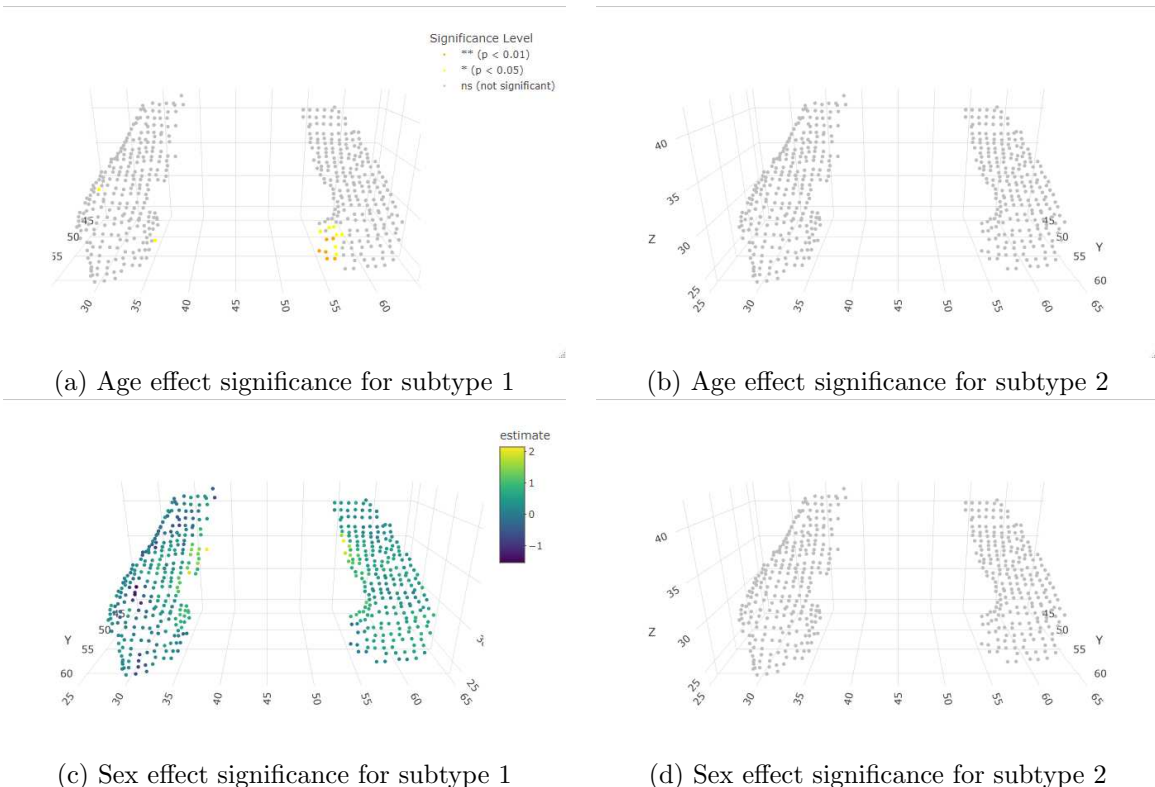


Figure S3: Spatial distribution of age and sex effects.

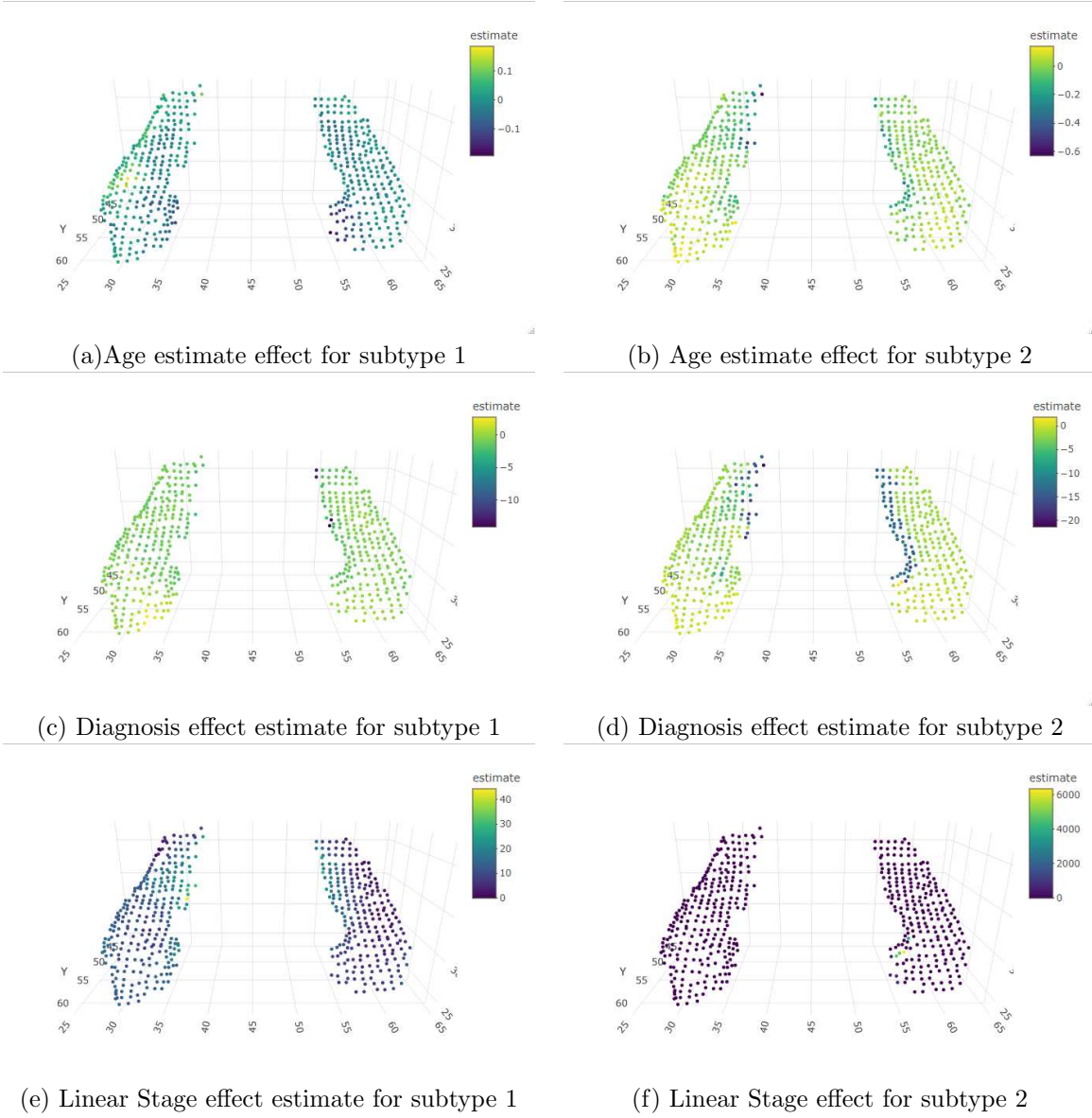


Figure S4: Spatial distribution of covariate-associated effects on hippocampal tau coverage across SuStaIn subtypes. Each panel displays estimated voxel-wise effects (standardized beta coefficients) of age, diagnosis, and SuStaIn stage on hippocampal tau coverage, modeled separately within subtype 1 (left column) and subtype 2 (right column). Notably, age and stage effects show consistent spatial gradients within each subtype, while diagnosis effects differ substantially between subtypes. Subtype 2 exhibits stronger and more localized diagnosis-related effects compared to subtype 1, where diagnosis appears to have limited influence on hippocampal tau distribution. These findings highlight subtype-specific spatial patterns and covariate sensitivities in tau deposition.

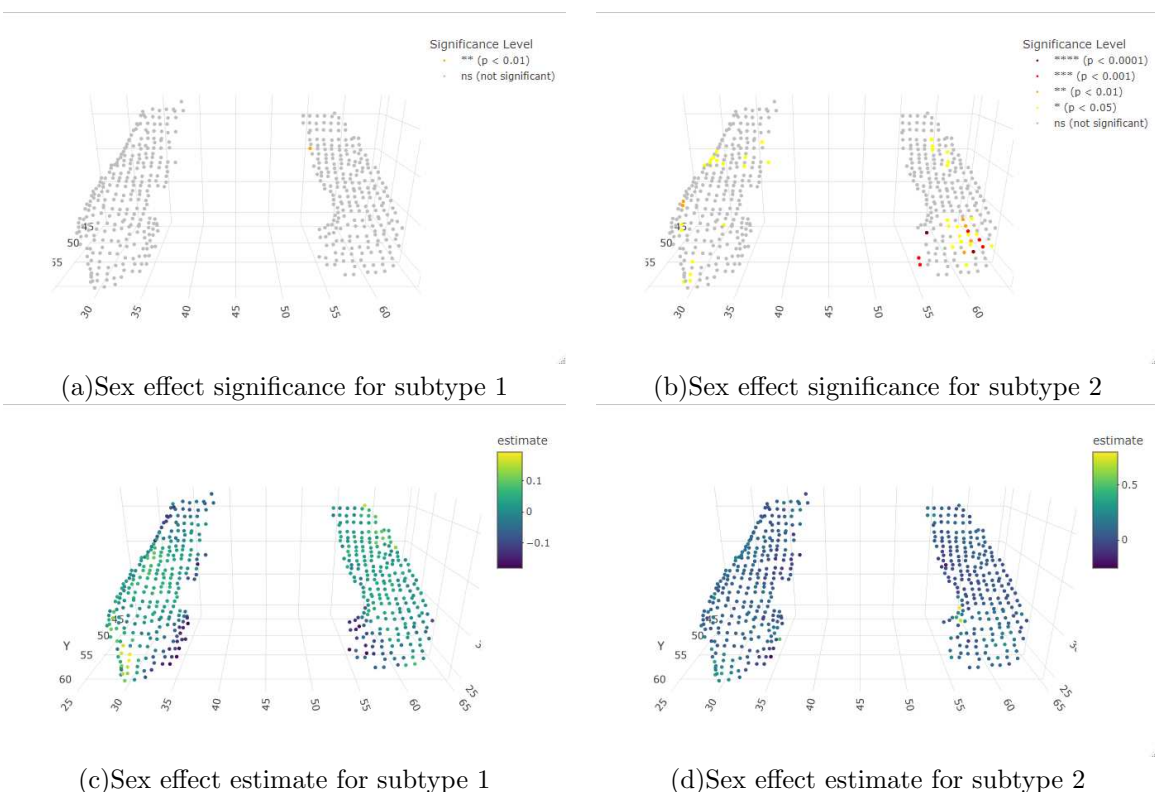


Figure S5: Supplementary Figure. Sex-related effects on hippocampal tau SUVR. (a–b) Significance maps for the effect of sex in subtypes 1 and 2. (c–d) Corresponding regression coefficient estimates for each subtype.

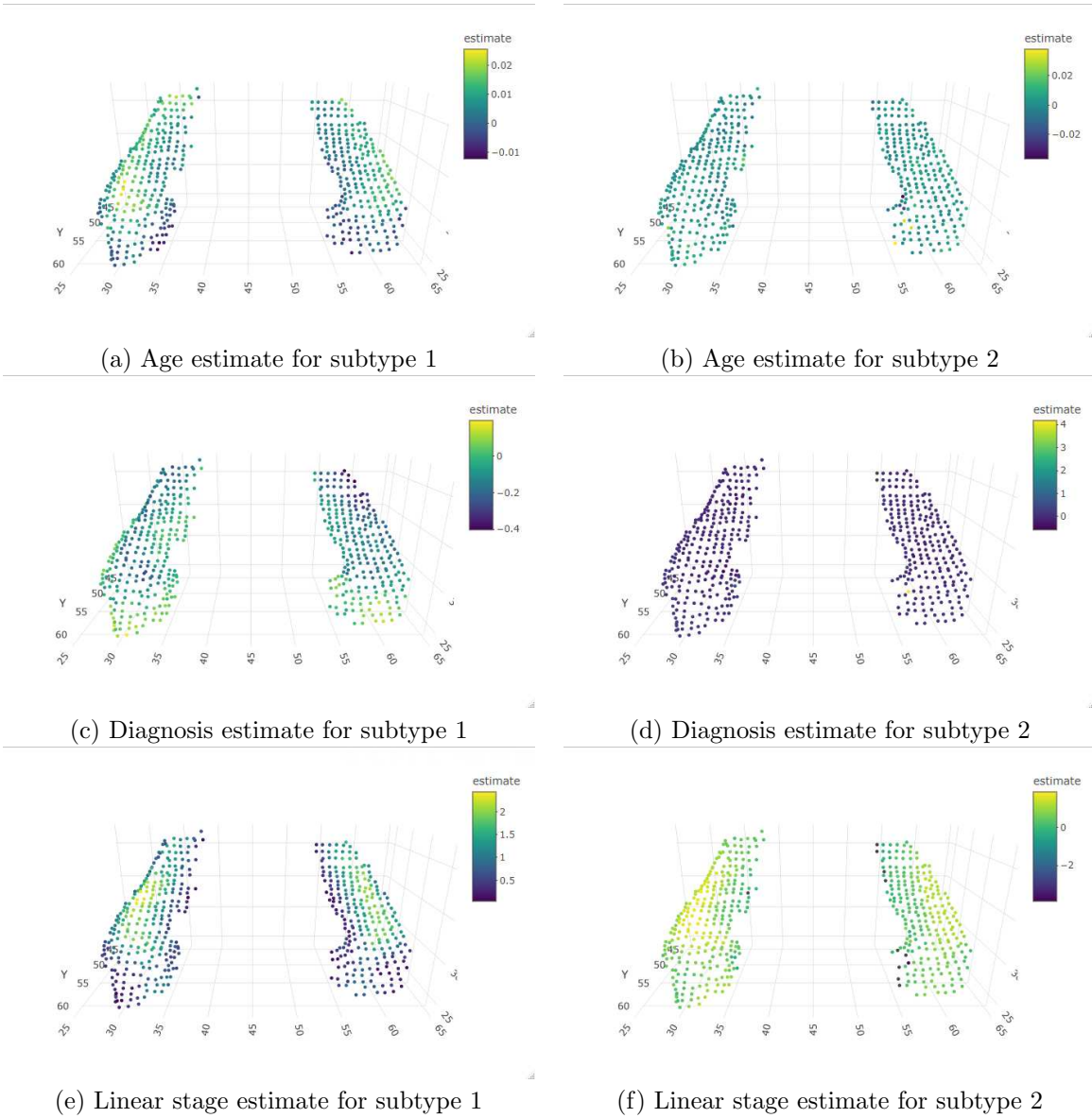


Figure S6: Supplementary Figure. Regression coefficient estimates for covariate effects on hippocampal tau SUVR. (a–b) Age effect estimates. (c–d) Diagnosis effect estimates. (e–f) Linear stage effect estimates, shown separately for subtypes 1 and 2.

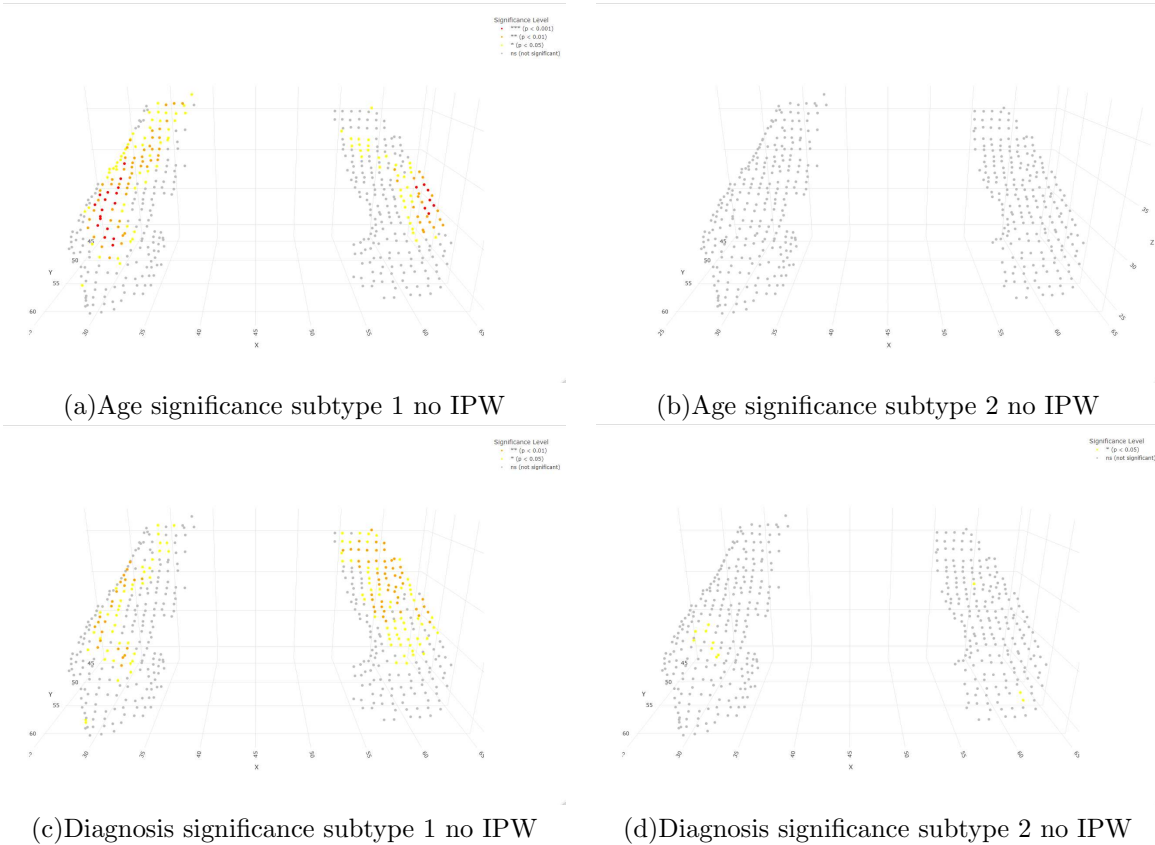


Figure S7: Supplementary Figure. Age and Diagnosis-related effects on hippocampal tau SUVR. (a–b) Significance maps for the effect of Age in subtypes 1 and 2 without IPW. (c–d) Significance maps for the effect of Diagnosis in subtypes 1 and 2 without IPW.

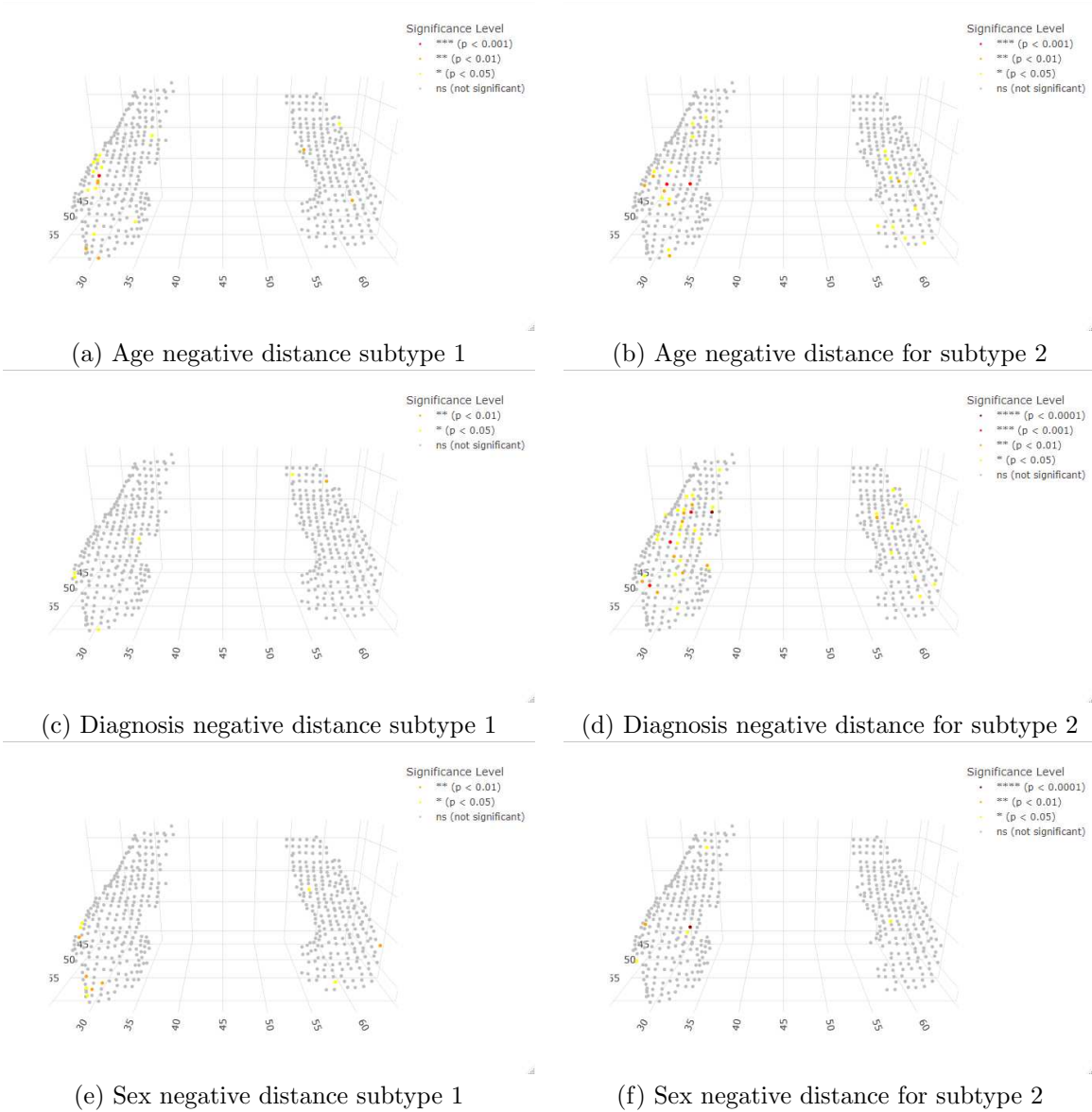


Figure S8: Thickness of age and diagnosis effects.

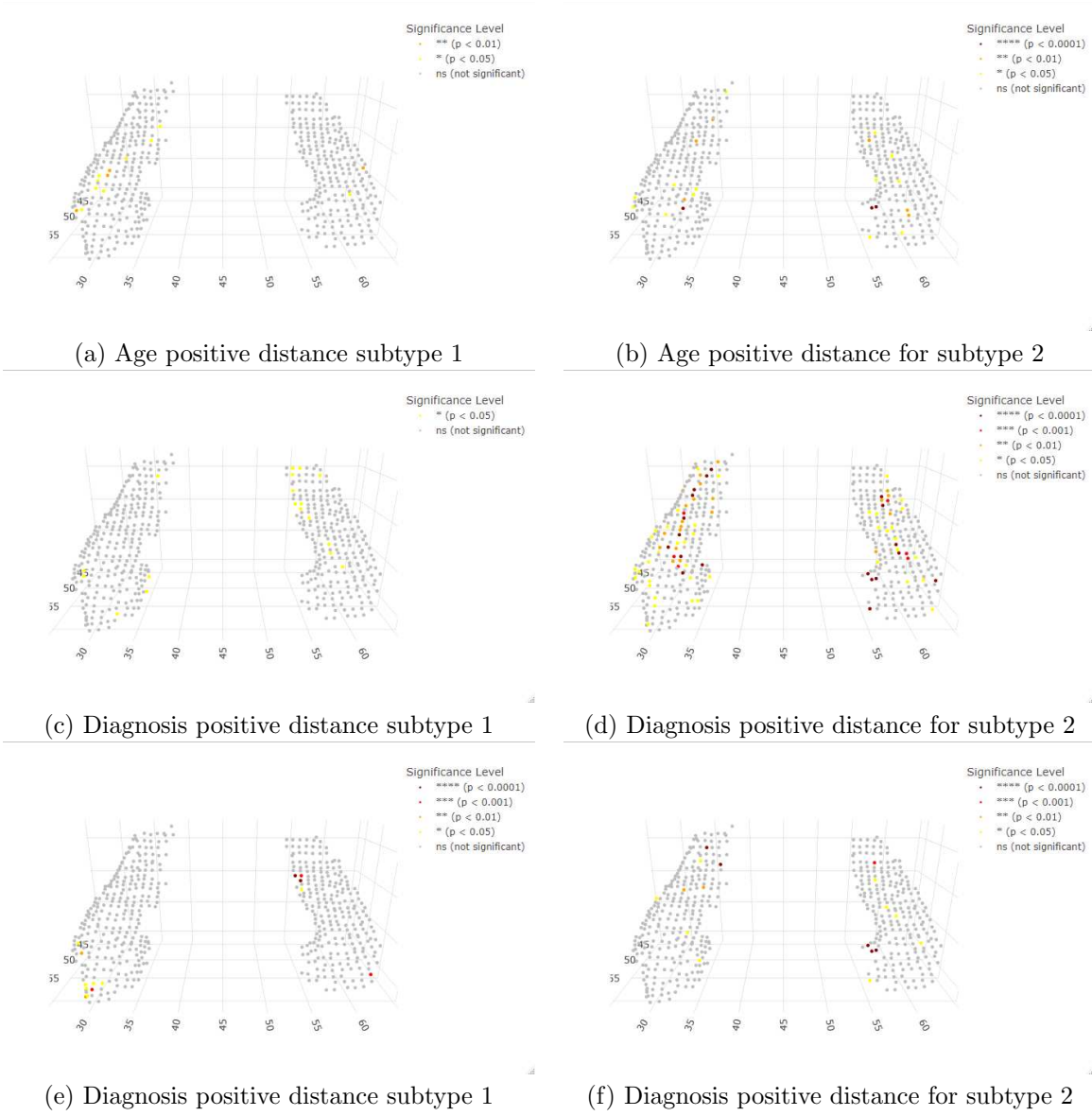


Figure S9: Thickness of age and diagnosis effects.

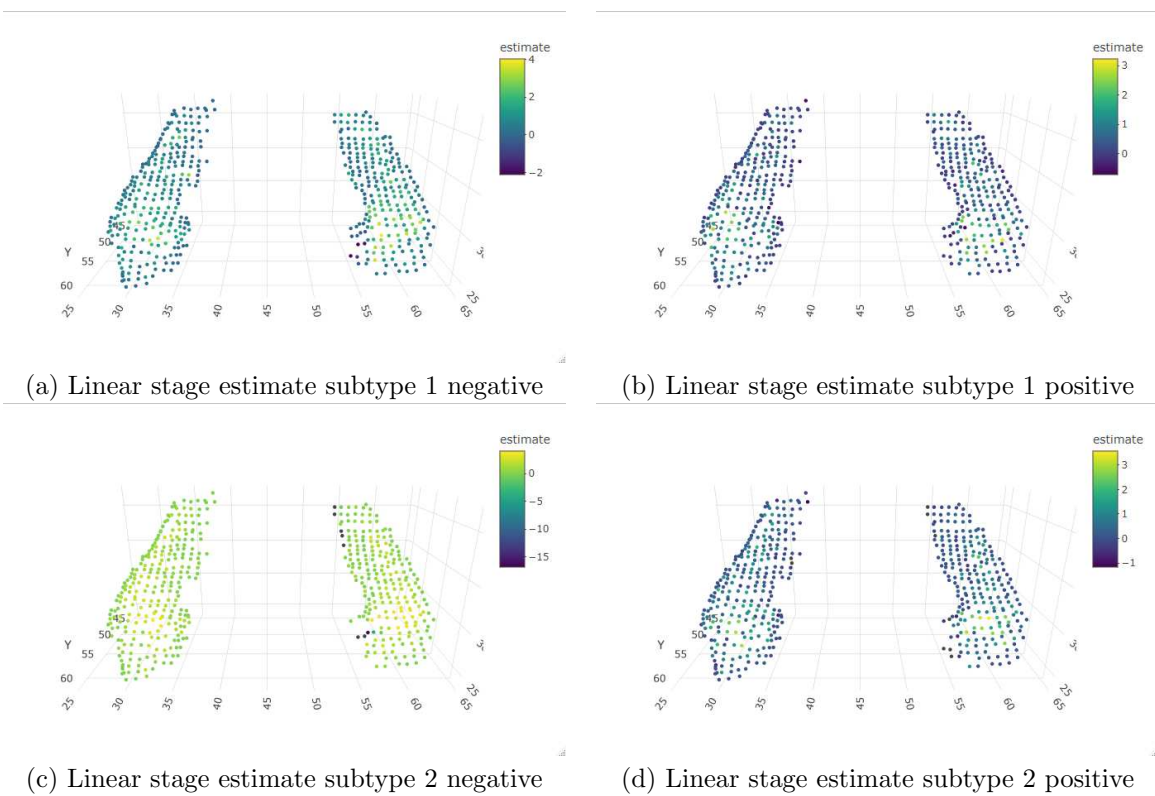


Figure S10: Supplementary Figure. SuStaIn stage effects on hippocampal tau deposition thickness, modeled via projection distance features. (a-d) Linear stage coefficient estimates for subtypes 1 and 2, shown separately for negative and positive projection directions.

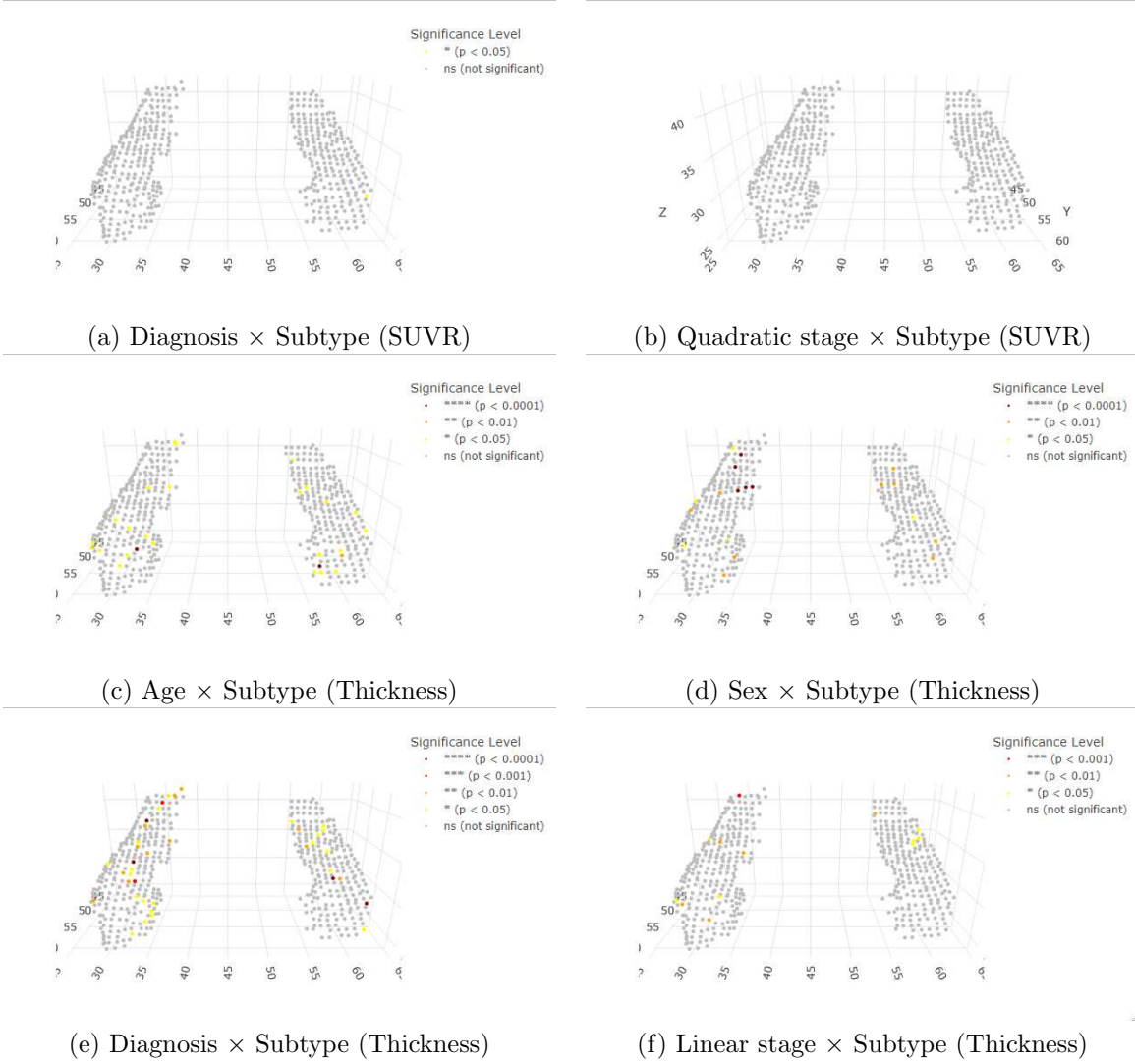


Figure S11: Significance maps for covariate-by-subtype interaction terms in the unified regression model. Each map displays surface regions where the effect of a covariate on tau deposition differs significantly between subtypes. (a) Significance of the diagnosis effect interaction on SUVR intensity; (b) Interaction significance for SuStaIn stage (quadratic term) on SUVR intensity; (c) Interaction significance of age on positive projection thickness; (d) Interaction significance of sex on positive projection thickness; (e) Interaction significance of diagnosis on positive projection thickness; (f) Interaction significance of SuStaIn stage (linear term) on positive projection thickness. All maps display  $-\log_{10}(p)$  values from IPW-adjusted regression models, with multiple significance levels indicated by color intensity. Benjamini–Hochberg correction was applied across all vertices to control for multiple comparisons.

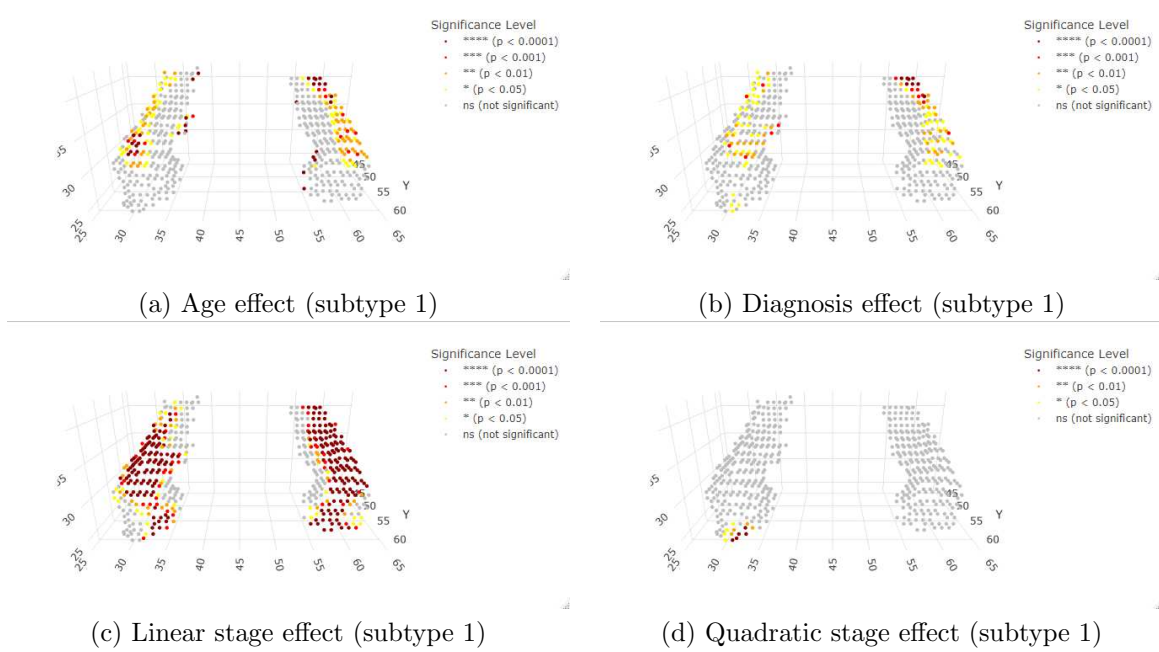
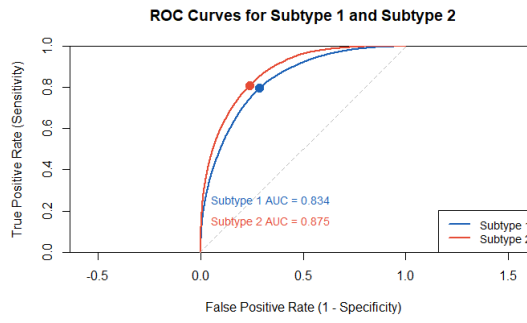


Figure S12: Voxelwise regression significance maps for subtype 1, displayed in MNI coordinate space. Each map shows the spatial distribution of covariate effects on SUVR at individual voxel locations without thresholding or projection onto surface geometry. (a–d) depict the significance of regression coefficients for age, diagnosis, linear SuStaIn stage, and quadratic SuStaIn stage, respectively. Statistical testing was performed at each voxel using linear regression, and  $p$ -values were corrected for multiple comparisons using the Benjamini–Hochberg (BH) procedure. These maps provide a conventional voxelwise baseline for comparison with our surface-based modeling framework.



(a) ROC curves for tau coverage

Figure S13: Model-based prediction of tau deposition shapes across SuStaIn stages using two-stage regression. (a) ROC curves for pointwise logistic models of tau coverage in subtype 1 and subtype 2, evaluated across all selected surface points and subjects. The models achieved high discriminative performance (AUC = 0.834 for subtype 1, 0.875 for subtype 2).

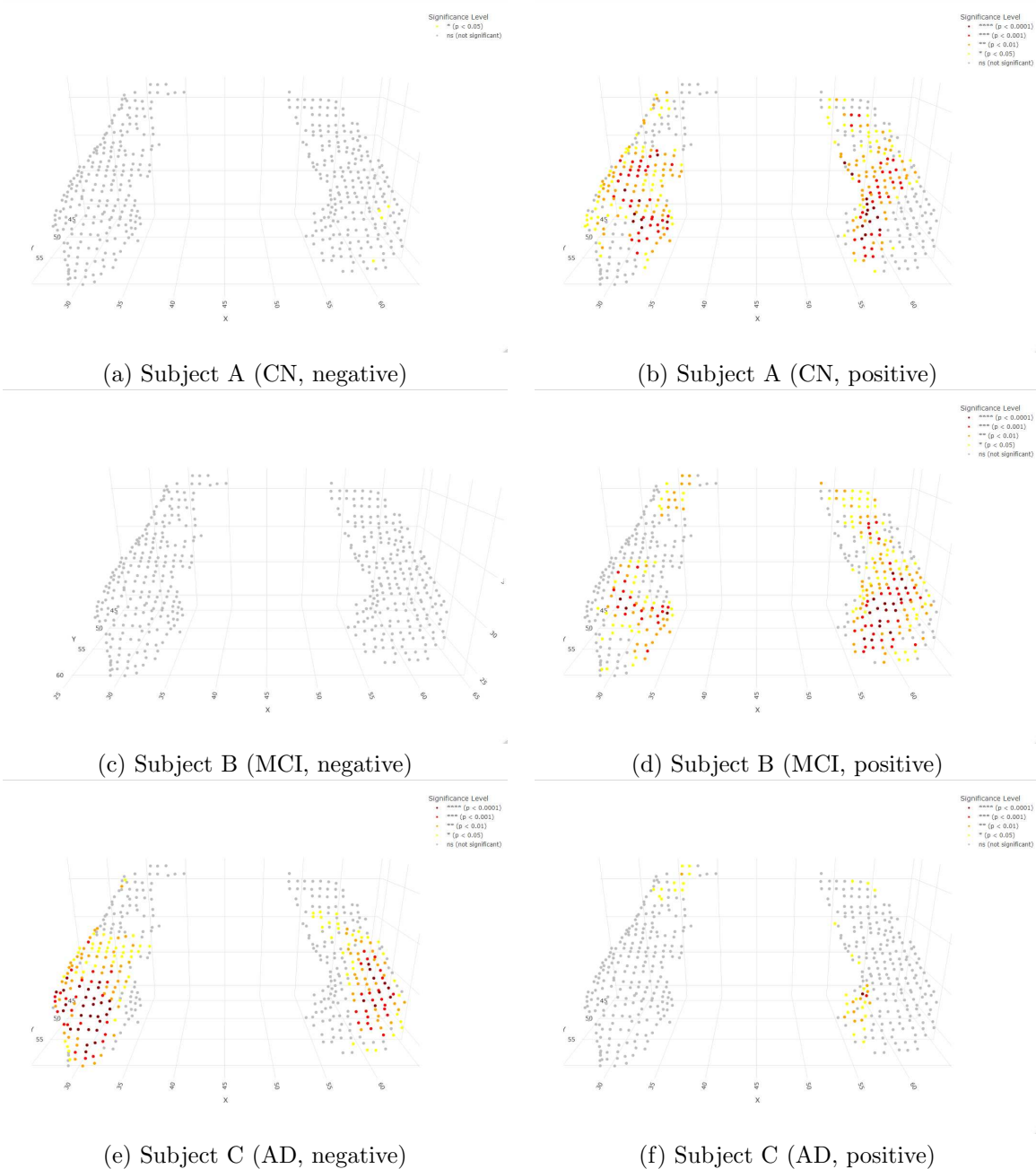


Figure S14: **Subject-Level Contamination Significance Maps.** Left: significance of negative contamination; Right: significance of positive contamination. Participants are shown in order of increasing hippocampal tau burden. Positive contamination is prominent in CN and MCI, whereas negative contamination emerges in AD.

## 2 External Validation using Amyloid Scans

### 2.1 Data Source and Preprocessing

**Sample characteristics** In the analysis, we included PET-MRI pairs from 611 participants from the ADNI study, each with T1-weighted MRI acquired within two years of the corresponding amyloid PET scan. Of these, 129 were cognitively normal (CN), 412 had mild cognitive impairment (MCI), and 70 were diagnosed with Alzheimer’s disease (AD). The sample included 276 males and 335 females, with a mean age of 74.6 years (SD = 7.8, range = 56.4–97.5 years). Table S1 describes the general demographic characteristics by study group for the participants included in the final sample.

Table S1: Demographic characteristics of the participants included in the study, stratified by diagnostic group. Values are presented as mean (standard deviation) for continuous variables and count (percentage) for categorical variables. APOE4 carrier status was derived from APOE genotypes (Missing if either allele was NA/invalid; Carrier if A1=4 or A2=4; Non-carrier otherwise).

	CN (N=129)	MCI (N=412)	AD (N=70)	Total (N=611)
<b>Age (years)</b>				
Mean (SD)	76.6 (7.1)	73.7 (7.8)	76.1 (8.0)	74.6 (7.8)
Median [Min, Max]	76.7 [56.4, 92.0]	73.4 [56.6, 97.5]	77.4 [57.1, 91.4]	74.9 [56.4, 97.5]
<b>Sex</b>				
Female	66 (51.2%)	174 (42.2%)	36 (51.4%)	276 (45.2%)
Male	63 (48.8%)	238 (57.8%)	34 (48.6%)	335 (54.8%)
<b>APOE <math>\epsilon</math>4 Carrier</b>				
Non-carrier	99 (76.7%)	248 (60.2%)	24 (34.3%)	371 (60.7%)
Carrier	30 (23.3%)	164 (39.8%)	46 (65.7%)	240 (39.3%)
Missing	0 (0%)	0 (0%)	0 (0%)	0 (0%)

**Image acquisition and preprocessing** All scans were pre-processed following the standard ADNI pipeline. Acquisition protocols for MRI and PET, as well as details on pre-processing procedures are described in detail at <https://adni.loni.usc.edu/>. Briefly, amyloid PET images were first co-registered to the corresponding native-space T1-weighted MRI, and then non-linearly warped to the MNI152 template space to ensure consistent anatomical alignment across subjects. For this analysis SUVR images were computed using the cerebellar gray matter as the reference region, applied uniformly across tracers (PiB/AV45/FBB), and partial volume correction was applied to reduce spill-over effects. A random subset of images from each scanner model was visually inspected to verify registration quality and confirm the absence of major motion artifacts. To account for potential site-related variability, we applied the Neuro-Combat algorithm to correct for scanner- and protocol-induced batch effects. Scans were grouped by scanner model, with rare models (fewer than five scans) merged by manufacturer. Age, sex, and diagnosis were included as biological covariates in the harmonization model to preserve meaningful variance while removing non-biological noise.

**Hippocampal Structure and Amyloid Signal Definition** For spatial localization, hippocampal geometry was defined using the MNI152-space T1-weighted MRI Automated Anatomical Labeling (AAL) atlas. The hippocampal region in this atlas was used to construct a medial surface representation, which served as a shared spatial surface for projecting amyloid PET signals. Because hippocampal  $A\beta$  signal is typically low and PET measurements are confounded by adjacent choroid-plexus uptake, we treat this as an external validation of the projection pipeline rather than a canonical amyloid topography analysis. To identify regions with elevated amyloid deposition, we applied a fixed thresholding procedure to each participant’s

PET SUVR image. Voxels with SUVR values exceeding 1.1 were considered amyloid-positive, this cutoff was chosen from our cohort-level SUVR distributional analysis. This subject specific binary mask was then projected onto the medial hippocampal surface for downstream shape based analysis. The SuStaIn modeling followed the same implementation as in the tau analysis, with the amyloid mask defined by the 1.1 SUVR cutoff.

## 2.2 Results

**SuStaIn-Derived Subtypes and Disease Staging** As an external pipeline validation on hippocampal projections, we applied the same SuStaIn implementation used for tau to the amyloid data. To avoid overinterpretation, we did not enforce correspondence between the amyloid derived subtype labels and the canonical tau phenotypes (i.e., limbic-dominant, posterior occipitotemporal, parietal-dominant/MTL-sparing, left-temporal); labels here are analysis specific. Subject specific masks used a fixed cutoff of  $SUVR = 1.1$ ; participants with no hippocampal voxels with  $SUVR \geq 1.1$  were labeled stage 0 (subtype 0). The cohort split into subtype 0 ( $n = 312$ ) and four nonzero subtypes ( $n = 101, 98, 88, 12$  for subtypes 1–4). Subtypes 1, 2 and 3 span a wide range of stages and include mostly CN and MCI individuals, while subtype 4 is smaller and more skewed toward later stages and AD diagnosis (Fig. S15). Given the limited sample size and reduced clinical variability of subtype 4, all subsequent analyses focus on subtypes 1, 2, and 3, which represent the dominant patterns of hippocampal amyloid accumulation in this cohort.

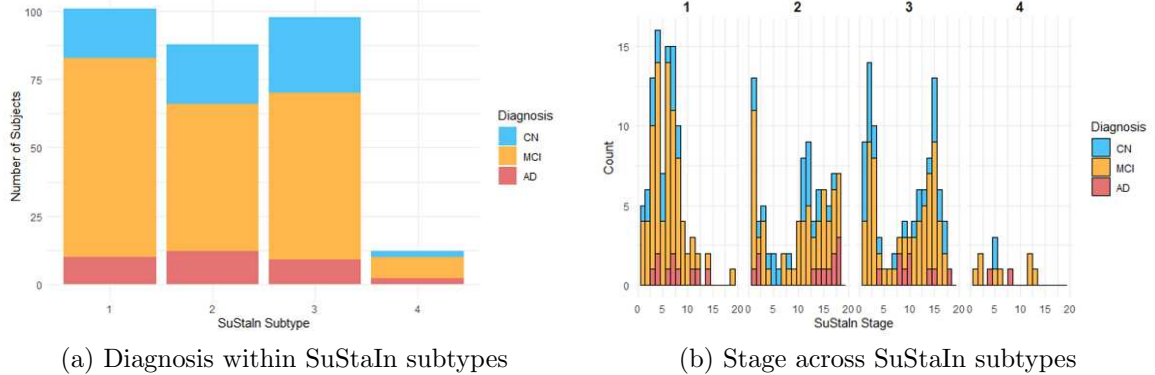


Figure S15: Overview of SuStaIn-derived subtypes (a) Diagnosis composition (CN, MCI, AD) within each subtype, shown as a stacked bar plot. (b) Distribution of SuStaIn stages within each subtype, stratified by diagnosis. Subtypes 1, 2 and 3 are predominantly early to mid-stage with a higher proportion of CN and MCI cases, while subtypes 4 are mid to later stage with more MCI and AD cases.

**Pointwise Coverage of Amyloid Deposition on the Hippocampal Surface** Similar to the tau analysis, we examined spatial coverage patterns using the logistic regression model. The number of scans in which each surface point was covered is visualized in (Fig. S16 a-c) for subtype 1-3 respectively. In all plots, the surface is displayed with anterior at the bottom and posterior at the top, with the right hippocampus on the left and the left hippocampus on the right, matching a brain orientation facing the viewer. Coverage is spatially non-uniform with focal clusters on the hippocampal surface. The right hippocampus generally shows higher coverage than the left, with peaks centered in the lateral/central body. Subtypes 1 and 3 produce the right-dominant pattern and subtype 2 shows a similar but more spatially restricted hotspot.

We next evaluated how coverage patterns were modulated by covariates. (Fig. S16 d-f) display significance maps for the logistic regression coefficients associated with diagnosis and SuStaIn stage in all three subtypes. Diagnosis shows no significance or spatially distinct effect. Thus, within subtypes, clinical diagnosis is not a reliable predictor of suprathreshold hippocampal amyloid coverage. SuStaIn stage was also included in the model to account for variation along the disease progression axis. To reflect its ordinal nature (20

levels), stage was encoded as a second-order polynomial. Both the linear and quadratic components are shown in (Fig. S16 g-l). The linear component (Fig. S16 g-i) indicates that advancing stage increases the probability of suprathreshold amyloid coverage as effects in subtypes 2 and 3 show strong signals over the right lateral/mid-anterior hippocampal surface with smaller patches on the left (medial/posterior); whereas subtype 1 shows weaker signals in the right lateral/posterior and left anterior regions. By contrast, the quadratic term (Fig. S16 j-l) shows no significant effect.

**Covariate Effects on Amyloid Deposition Intensity (SUVR)** We evaluated the effects of age, diagnosis, and SuStaIn stage on hippocampal amyloid SUVR, separately within each subtype. The significance maps are shown in (Fig. S17). For age related effects (Fig. S17 a-c) no surface locations are significant in subtype 1, and only a few isolated vertices appear in subtypes 2 and 3 with small, inconsistent signs and no coherent spatial pattern. Diagnosis effects were predominantly observed in subtype 3 (Fig. S17 d-f). Significant regions are localized to the right anterior-to-posterior medial surface and no effects are evident on the left hippocampus. In subtype 1 and 2 there were no significant regions indicating no spatially coherent diagnosis effect on hippocampal amyloid SUVR in these subtypes. Linear SuStaIn stage effects showed strong and widespread significance in subtypes 1 and 3 (Fig. S17 g-i), with clusters concentrated along the right hippocampal medial surface and extending anterior-to-posterior. Subtype 2 exhibits scattered, small clusters. In Quadratic stage terms (Fig. S17 j-l) a few localized patches appear in subtype 1 and 2 while subtype 3 show no statistically significant vertices.

**Stage-Dependent Effects on Tau Deposition Thickness** To capture shape-level changes in amyloid pathology beyond intensity or coverage, we analyzed a geometric measure of deposition thickness based on projection distance. Linear stage effects were observed in subtypes 2 and 3 and across both projection directions whereas subtype 1 shows insignificant effect (Fig. S18 a-f). In subtype 2 and 3, the spatial pattern of significance was nearly identical between the positive and negative features, indicating that amyloid thickness increases occur symmetrically around the principal surface. Quadratic effects were weak (Fig. S18 g-l), a few localized data points were observed with no spatial pattern.

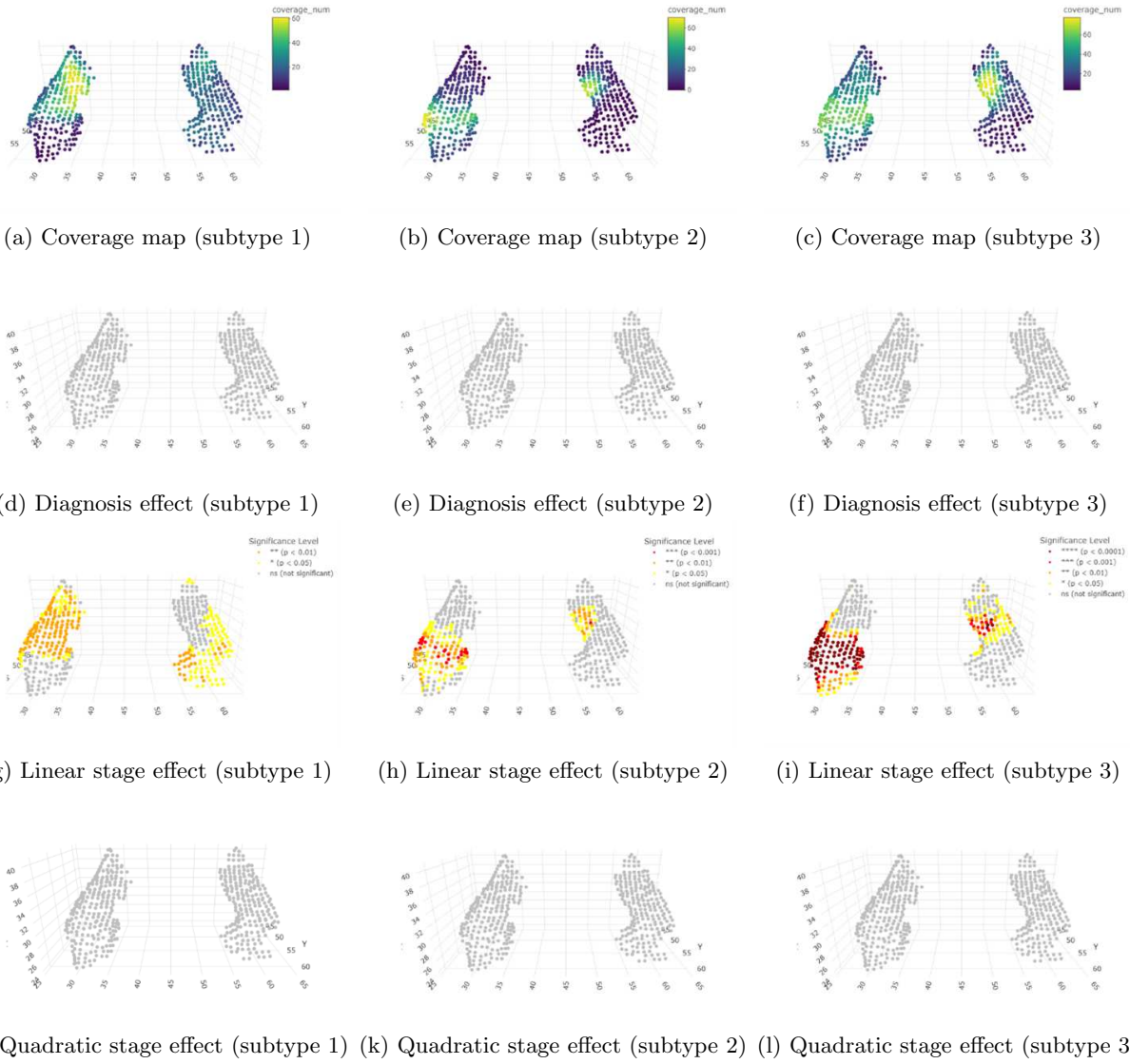


Figure S16: Coverage and significance maps for covariate effects on suprathreshold amyloid signal across the hippocampal surface. Panels (a-c) display the number of scans showing suprathreshold signal  $SUVR \geq 1.1$  at each surface location for subtype 1, subtype 2, and subtype 3 respectively. Panels (d-f) show no significant diagnosis effect on amyloid coverage, estimated using IPW-adjusted logistic regression. Panels (g-i) depict the significance of the linear SuStaIn stage effect, and panels (j-l) depict the quadratic SuStaIn stage effect, which are not significant. Here, the “linear” and “quadratic” components correspond to the first two orthogonal polynomial terms.

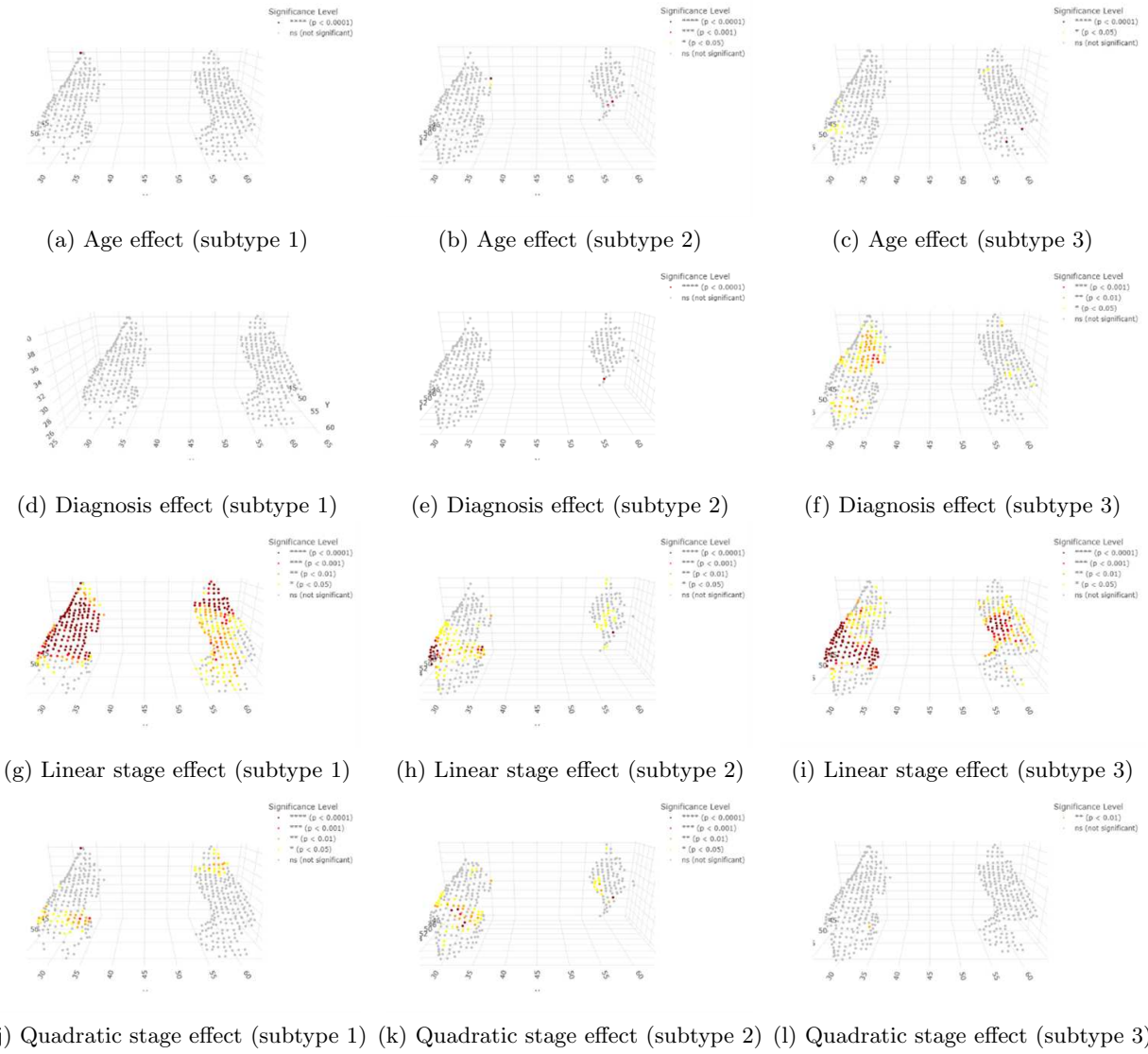


Figure S17: Significance maps of covariate effects on hippocampal amyloid SUVR. (a–c) Age-related effects show a very tiny significant cluster in the right lateral part of hippocampus of subtype 3 with few scattered vertices in subtype 2. (d–f) Diagnosis related effects are stronger in subtype 3 and non-significant in subtypes 1 and 2. (g–l) SuStaIn stage, linear effect is widespread in subtype 1, 3 and Subtype 2 exhibits scattered, small clusters. Quadratic stage terms show a few localized patches in subtype 1 and 2 while subtype 3 is statistically non-significant. Here, we excluded vertices whose per vertex IPW SUVR model could not be estimated.

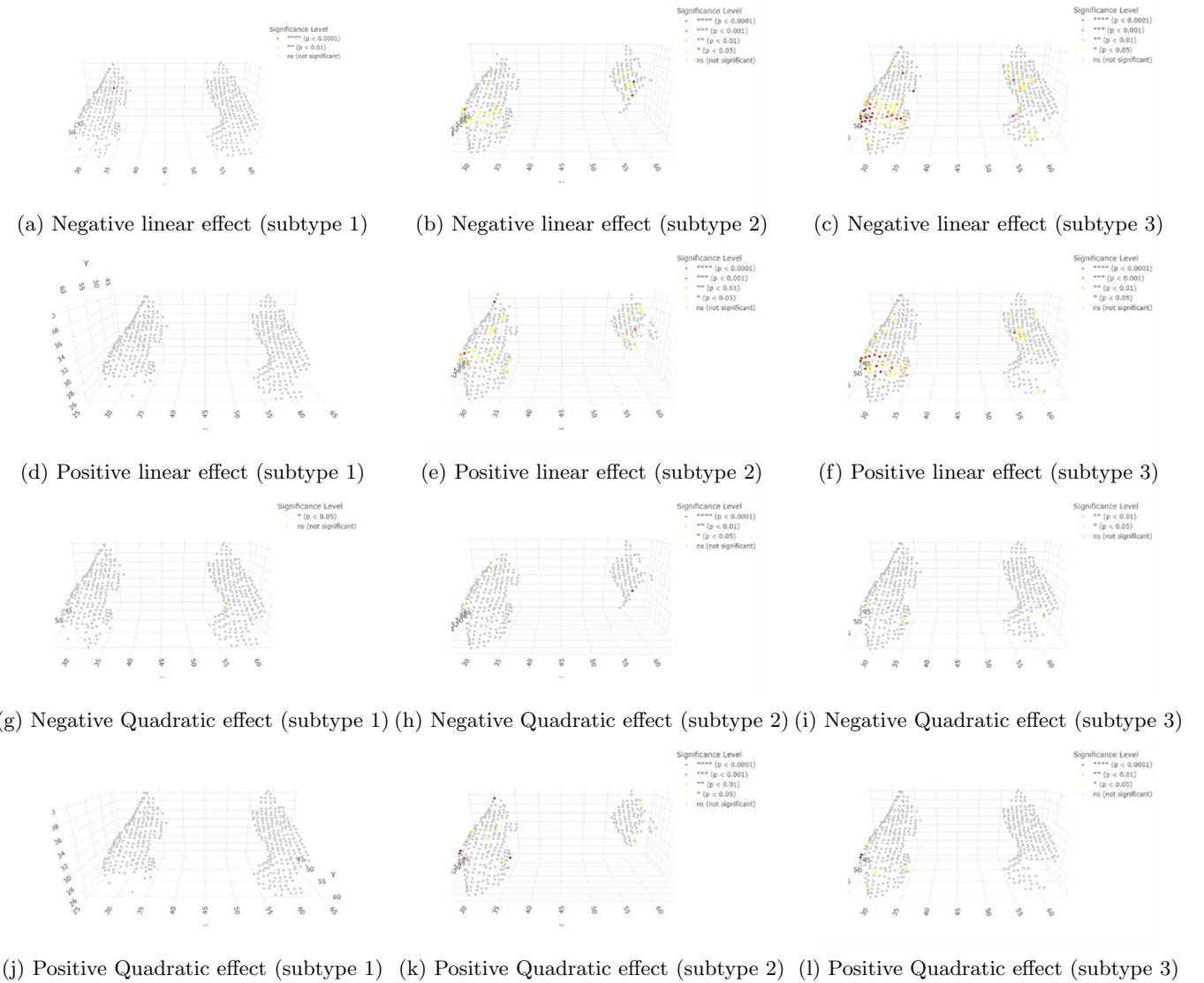


Figure S18: Significance maps of SuStaIn stage effects on hippocampal amyloid deposition thickness, separated by subtype, projection direction, and polynomial term. Each panel shows results from an IPW-adjusted regression model fit within a specific subtype. Panels (a–f) correspond to negative-direction projection distances; (g–l) show positive-direction thickness. All maps display  $-\log_{10}(p)$  values thresholded at multiple significance levels after BH correction for multiple comparisons. Subtype labels are indicated in parentheses for consistency with other figures. Here, we excluded vertices whose per vertex IPW SUVR model could not be estimated.